

Single- versus Multi-Carrier Terahertz-Band Communications: A Comparative Study

Simon Tarboush, Hadi Sarieddeen, *Member, IEEE*, Mohamed-Slim Alouini, *Fellow, IEEE*
and Tareq Y. Al-Naffouri, *Senior Member, IEEE*

Abstract—The prospects of utilizing single-carrier (SC) and multi-carrier (MC) waveforms in future terahertz (THz)-band communication systems remain unresolved. On the one hand, the limited multi-path components at high frequencies result in frequency-flat channels that favor low-complexity wideband SC systems. On the other hand, frequency-dependent molecular absorption and transceiver characteristics and the existence of multi-path components in indoor sub-THz systems can still result in frequency-selective channels, favoring off-the-shelf MC schemes such as orthogonal frequency-division multiplexing (OFDM). Variations of SC/MC designs result in different THz spectrum utilization, but spectral efficiency is not the primary concern with substantial available bandwidths; baseband complexity, power efficiency, and hardware impairment constraints are predominant. This paper presents a comprehensive study of SC/MC modulations for THz communications, utilizing an accurate wideband THz channel model and highlighting the various performance and complexity trade-offs of the candidate schemes. Simulations demonstrate that discrete-Fourier-transform spread orthogonal time-frequency space (DFT-s-OTFS) achieves a lower peak-to-average power ratio (PAPR) than OFDM and OTFS and enhances immunity to THz impairments and Doppler spreads, but at an increased complexity cost. Moreover, DFT-s-OFDM is a promising candidate that increases robustness to THz impairments and phase noise (PHN) at a low PAPR and overall complexity.

Index Terms—THz Communications, CP-OFDM, SC-FDE, DFT-s-OFDM, OQAM/FBMC, OTFS, DFT-s-OTFS.

I. INTRODUCTION

THE successful deployment of millimeter-wave (mmWave) communications [1] has encouraged researchers to explore the last piece of available spectrum, the terahertz (THz) band over 0.3 – 10 THz, which promises to be an essential ingredient of future ultra-broadband wireless communications [2], [3]. Moving towards beyond-fifth generation (B5G) and sixth-generation (6G) wireless networks [4], [5], a plethora of services are expected to be supported [6], such as ultra-low latency communications, ubiquitous connectivity, and very high data rates (up to several terabits-per-second (Tbps)). Such features can be leveraged in novel use cases in fixed radio links, wireless local area networks, nano cells, or inter-chip communications. Furthermore, accurate localization, sensing, and imaging applications are promised in the THz band

S. Tarboush is a researcher from Damascus, Syria (e-mail: simon.w.tarboush@gmail.com). The rest of the authors are with the Department of Computer, Electrical and Mathematical Sciences and Engineering (CEMSE), King Abdullah University of Science and Technology (KAUST), Thuwal, Makkah Province, Kingdom of Saudi Arabia, 23955-6900 (e-mail: hadi.sarieddeen@kaust.edu.sa; slim.alouini@kaust.edu.sa; tareq.alnaffouri@kaust.edu.sa).

[7], [8]. However, researchers should first overcome several challenges in THz materials and technologies (photonic and electronic) and the corresponding system designs and hardware complexity [9], [10].

The THz-band channel's peculiarities (frequency/distance-dependency and sparsity) impose challenging constraints on the physical layer of future wireless standards. THz signals suffer from severe path loss, which limits the transmission distances to a few meters [11]. However, long distance sub-THz communications (over hundreds of meters) are still feasible with high-gain antenna arrays [12]. The frequency-selective molecular absorption further results in distance-dependent spectrum fragmentation and shrinking (variable-bandwidth transmission windows) [13]. Hence, ultra-massive multiple-input multiple-output (UM-MIMO) antenna arrays and intelligent reflecting surfaces (IRSs) are essential for extending the THz communication range [13]–[15]. Furthermore, since the line-of-sight (LoS) path dominates THz-band signal propagation, THz channels tend to be flat-fading. However, a few multi-path components might persist, especially in indoor scenarios, resulting in frequency-selective channels (FSCs) of coherence bandwidths of hundreds of megahertz (MHz) over medium communication distances [16]. Therefore, THz multi-carrier (MC) schemes retain scenario-specific benefits.

Designing efficient THz-specific waveforms is crucial for unleashing the THz-band's true capabilities. Because bandwidth and spectral efficiency (SE) are not yet a THz bottleneck; low complexity, robustness to hardware impairments and Doppler spreads, and high power efficiency are prioritized. The first sub-THz standard (IEEE 802.15.3d [17]) supports switched point-to-point connectivity with data rates exceeding 100 Gbps, offering two modes: (1) single-carrier (SC) modulation (long-range; high-rate) and (2) on-off keying (OOK) (low-complexity; short-range). OOK utilizes femtosecond-long pulses that could span an ultra-wideband THz spectrum [18]. However, temporal broadening [16] and the challenging synchronization procedure question the feasibility of pulse-based modulation. IEEE 802.15.3d-compliant waveforms are proposed in [19], where novel pulse-shaping designs reduce out-of-band (OOB) emissions. Several other projects revisit the physical layer for future B5G sub-THz systems. Most notably, the BRAVE project [20] advocates for modified SCs schemes, such as continuous phase modulated single-carrier frequency-division multiple-access (CPM SC-FDMA), constrained envelope CPM-SC, differential modulation (like differential phase-shift keying), SC with optimized polar modulation (robust to phase noise (PHN)) [21], and variations

of spatial- and index-modulation [22]–[24]. Block-based SC waveforms, such as discrete-Fourier-transform spread OFDM (DFT-s-OFDM) [25] can also be investigated.

A variety of THz MC schemes can be explored. In the simplest form, multiple (quasi)-orthogonal non-overlapping SC modulations can be combined with some form of carrier aggregation [26]. Cyclic-prefix orthogonal frequency-division multiplexing (CP-OFDM) is well investigated, but it is discouraged at THz [27], [28] due to its strong spectral leakage (high OOB emissions), unfavorable peak-to-average power ratio (PAPR) properties (limitations in state-of-the-art THz power amplifiers (PAs) [29]), strict synchronization procedures, and high sensitivity to Doppler spread. Other MC schemes such as novel fifth-generation new-radio (5G-NR) filter-based candidates provide their prospects and challenges. Such filtering is on the whole band in filtered-OFDM (f-OFDM) [30], per-subband (a set of contiguous subcarriers) in universal filtered multi-carrier (UFMC) [31], or per-subcarrier in offset quadrature amplitude modulation-based filter-bank multi-carrier (OQAM/FBMC) [32] and generalized frequency-division multiplexing (GFDM) [33]. Although filter-based schemes overcome some CP-OFDM limitations, reducing OOB emissions and enhancing SE, their high PAPR characteristics and increased implementation complexity can be prohibitive in Tbps baseband systems. For example, the single-tap equalizer is no longer sufficient with CP-free OQAM/FBMC, requiring more complex equalization. Other works propose windowed overlap-and-add OFDM (WOLA-OFDM) [34], or combinations such as OQAM/GFDM [35].

THz-specific multiple-access techniques are also emerging, such distance-adaptive MCs [27], hierarchical-bandwidth modulations [28], and distance-/frequency-dependent adaptive CP-OFDM [36], which optimize distance-dependent spectral window utilization. Spatial-spread orthogonal frequency-division multiple-access (SS-OFDMA) is another THz MC candidate that realizes frequency-based beam spreading by allocating subcarriers for users in different directions [37]. Similarly, beam-division multiple-access (BDMA) [38] schedules mutually non-overlapping beam subsets for users, followed by relaxed per-beam synchronization. Moreover, THz-band non-orthogonal multiple access (NOMA) techniques are argued to be feasible, despite the narrow beams that make user clustering difficult [39]. Other conventional techniques that improve SE at a reduced power cost, PAPR, and transceiver complexity, are also being studied for THz communications, including spatial [15] and index modulation [40] paradigms.

Other novel waveforms target specific THz use cases and constraints. For instance, zero-crossing modulation [41] uses temporal oversampling and 1-bit quantization to relax hardware requirements, such as in the digital-to-analog converter (DAC) and analog-to-digital converter (ADC). Furthermore, orthogonal time-frequency space (OTFS) modulation [42] is tailored for time-variant (TV) channels and high Doppler spreads, which arise in high-speed THz communication scenarios such as vehicle-to-everything (V2X), drone, and ultra-high-speed rail communications. OTFS is superior in block error rate performance to CP-OFDM when assuming mmWave LoS V2X channels [43]; also when accounting for oscillator

PHN impairments [44]. To meet the THz integrated sensing and communication (ISAC) requirements, the utilization of DFT-s-OFDM, with some modifications, is discussed in [45]. Most recently, a novel scheme called DFT-s-OTFS is proposed [46], [47] to address the severe Doppler effects and PAPR challenges of THz ISAC.

Many performance metrics need to be considered when designing THz waveforms, such as bit error rate (BER), PAPR, and baseband computational complexity. Furthermore, hardware imperfections and radio frequency (RF) impairments critically impact THz waveform design, where candidate THz materials/hardware are still under development. Hardware imperfections include PA non-linearity, wideband in/quadrature-phase imbalance (IQI) [48], phase uncertainty in the phase-shifters (PSs) [49], and PHN (studied for SC schemes [50] and CP-OFDM [51] in sub-THz and THz [48] systems). THz channel-induced phenomena such as beam split and misalignment [52] are also critical, especially with UM-MIMO systems. Moreover, the synchronization becomes more challenging with carrier frequency offset (CFO) and symbol-timing offset (STO) at THz frequencies. Subcarrier spacing (SCS), its impact on PHN, and the design of phase-tracking reference signals are studied in [53], [54] to assess whether CP-OFDM and DFT-s-OFDM can support mmWave and sub-THz communications. Moreover, a THz SC frequency-domain equalization technique (SC-FDE) is developed in [48], and a pilot design strategy based on index modulation is proposed in [55]. SC systems are found superior to CP-OFDM in mmWave systems [56] when taking into account the transmitter PA nonlinearities. For indoor THz scenarios, SC-FDMA with linear equalization is shown to be superior to CP-OFDM and SC with linear-/decision-feedback-equalization [57].

The literature lacks a holistic and fair comparative study of THz-band SC/MC schemes, and this work attempts to fill this gap. We aim to analyze a plethora of candidate schemes to be able to draw recommendations on the suitable waveforms for specific THz use cases. The main contributions of this paper are summarized as follows:

- We study the THz compatibility of multiple modulation schemes, namely, SC-FDE, CP-OFDM, DFT-s-OFDM, OTFS, DFT-s-OTFS, and OQAM/FBMC, adopting our newly developed accurate THz channel model/simulator (TeraMIMO [52]).
- We analyze normalized SE, physical layer end-to-end (PH-E2E) latency, OOB emissions (reference THz IEEE 802.15.3d spectral mask), PAPR (theoretical bounds), and computational complexity.
- We provide a fair comparison of modulation schemes under THz-specific scenarios such as oscillator PHN (we study a Gaussian uncorrelated PHN model), mobility, and beam split.
- We promote DFT-s-OFDM and DFT-s-OTFS as promising schemes for future B5G/6G networks.

The remainder of this paper is organized as follows: We first introduce the system and channel models in Sec. II. Then, we present a general framework for analyzing the studied SC/MC schemes and key performance indicators (KPIs) in Sec. III.

Afterward, extensive simulation results validate our analyses in Sec. IV, where we recommend suitable waveforms for specific scenarios. We conclude in Sec. V. Regarding notation, non-bold lower case, bold lower case, and bold upper case letters correspond to scalars, vectors, and matrices: $a[n]$ denotes the n th element of \mathbf{a} and $\mathbf{a}[m]$ and $a[n, m]$ denote the m th column and the (n, m) th element of \mathbf{A} , respectively. \mathbf{I}_N is the identity matrix of size N , $\mathbf{0}_{N, M}$ is a zero matrix of size $N \times M$, and \mathbf{a}_N is a vector of size N . The superscripts $(\cdot)^T$, $(\cdot)^*$, $(\cdot)^H$, $(\cdot)^{-1}$, and $(\cdot)^n$ stand for the transpose, conjugate, conjugate transpose, inverse, and n th-power functions, respectively. $|\cdot|$ is the absolute value (or set cardinality), $\text{diag}(a_0, a_1, \dots, a_{N-1})$ is an $N \times N$ diagonal matrix of diagonal entries a_0, a_1, \dots, a_{N-1} , $\text{vec}(\mathbf{A})$ is the vectorized matrix representation that stacks the columns of \mathbf{A} in a single column, $\mathbb{E}(\cdot)$ is the expectation operator, and $\Pr(\cdot)$ is the probability density function. The notations \otimes , $[\cdot]_N$, $\langle \cdot, \cdot \rangle$, $\mathcal{R}(\cdot)$, and $j = \sqrt{-1}$ denote the Kronecker product, remainder modulo N , inner product, real part, and imaginary unit, respectively. The superscripts (t) and (r) denote transmitter (Tx) and receiver (Rx) parameters, respectively. $\mathcal{N}(\varphi, \sigma^2)$ is the distribution of a Gaussian random variable of mean φ and variance σ^2 , $\mathcal{CN}(\mathbf{a}, \Sigma)$ is the distribution of a complex Gaussian random vector of mean \mathbf{a} and covariance matrix Σ . The normalized N -point DFT and IDFT matrices are denoted by \mathbf{F}_N and \mathbf{F}_N^H , respectively. The used abbreviations are summarized in Tables VI and VII.

II. SYSTEM AND CHANNEL MODEL

We aim to evaluate the performance of candidate SC/MC schemes in realistic THz settings, including massive antenna dimensions and ultra-wide bandwidths. We adopt the array-of-subarrays (AoSA) architecture of TeraMIMO [52], in which each subarray (SA) is composed of many antenna elements (AEs), as depicted in Fig. 1. AoSAs can mitigate THz hardware constraints and combat the limited communication distance problem using low-complexity beamforming [10]. We assume $\mathcal{Q} = Q_a \times Q_b$ SAs, and $\bar{\mathcal{Q}} = \bar{Q}_a \times \bar{Q}_b$ tightly-packed directional AEs per SA. Each AE is attached to a wideband THz analog PS of acceptable phase error, return loss, and insertion loss [49] (such PSs can be implemented using graphene transmission lines in plasmonic solutions [58]). We assume the AoSAs to realize sub-connected hybrid beamforming, with analog beamforming over the AEs of each SA. Each RF chain thus drives one disjoint SA, reducing power consumption and complexity; the SAs provide the spatial diversity gain.

For SCs, we consider SC-FDE, DFT-s-OFDM, and DFT-s-OTFS. For MCs, we investigate CP-OFDM, OQAM/FBMC, and OTFS, assuming M -subcarriers. The m th-subcarrier Rx signal is

$$\tilde{\mathbf{y}}[m] = \mathbf{W}_{\text{BB}}^H[m] \mathbf{W}_{\text{RF}}^T \mathbf{H}[m] \tilde{\mathbf{x}}[m] + \mathbf{W}_{\text{BB}}^H[m] \mathbf{W}_{\text{RF}}^T \mathbf{n}[m], \quad (1)$$

where assuming perfect time and frequency synchronization (no STO or CFO), the received signal is processed using an RF combining matrix, $\mathbf{W}_{\text{RF}} \in \mathbb{C}^{\mathcal{Q}^{(r)} \bar{\mathcal{Q}}^{(r)} \times \mathcal{Q}^{(r)}}$, and a digital baseband combining matrix, $\mathbf{W}_{\text{BB}}[m] \in \mathbb{C}^{\mathcal{Q}^{(r)} \times N_{\text{tot}}}$; $\mathbf{n}[m] \in \mathbb{C}^{\mathcal{Q}^{(r)} \bar{\mathcal{Q}}^{(r)} \times 1}$ is the additive white Gaussian noise (AWGN) vector of independently distributed $\mathcal{CN}(\mathbf{0}_{\mathcal{Q}^{(r)} \bar{\mathcal{Q}}^{(r)}}, \sigma_n^2 \mathbf{I}_{\mathcal{Q}^{(r)} \bar{\mathcal{Q}}^{(r)}})$ elements of noise

power σ_n^2 . Note that $N_{\text{tot}} = N_{\text{st}} \times N$, where $N_{\text{st}} \leq \mathcal{Q}^{(t)}$ is the number of data streams ($\mathcal{Q}^{(t)}$ is also the number of Tx RF chains), and N is the number of MC symbols per frame.

The UM-MIMO channel matrix, $\mathbf{H}[m] \in \mathbb{C}^{\mathcal{Q}^{(r)} \bar{\mathcal{Q}}^{(r)} \times \mathcal{Q}^{(t)} \bar{\mathcal{Q}}^{(t)}}$, represents the overall complex channel at the m th-subcarrier; assuming a time-invariant (TIV)-FSC, \mathbf{H} can be expressed as

$$\mathbf{H}[m] = \begin{bmatrix} \mathbf{H}_{1,1}[m] & \cdots & \mathbf{H}_{1,\mathcal{Q}^{(t)}}[m] \\ \vdots & \ddots & \vdots \\ \mathbf{H}_{\mathcal{Q}^{(r)},1}[m] & \cdots & \mathbf{H}_{\mathcal{Q}^{(r)},\mathcal{Q}^{(t)}}[m] \end{bmatrix}, \quad (2)$$

where $\mathbf{H}_{q^{(r)},q^{(t)}}[m] \in \mathbb{C}^{\bar{\mathcal{Q}}^{(r)} \times \bar{\mathcal{Q}}^{(t)}}$ denotes the channel response between the $q^{(t)}$ th Tx SA and the $q^{(r)}$ th Rx SA. Further details on the channel model can be found in [52] and equations therein (Eqs. (15) and (16) define $\mathbf{H}_{q^{(r)},q^{(t)}}[m] \in \mathbb{C}^{\bar{\mathcal{Q}}^{(r)} \times \bar{\mathcal{Q}}^{(t)}}$ in the delay and frequency domains, respectively). The discrete-time Tx complex baseband signal at the m th-subcarrier is

$$\tilde{\mathbf{x}}[m] = \mathbf{P}_{\text{RF}} \mathbf{P}_{\text{BB}}[m] \mathbf{s}[m], \quad (3)$$

where $\mathbf{P}_{\text{BB}}[m] \in \mathbb{C}^{\mathcal{Q}^{(t)} \times N_{\text{tot}}}$ is the digital baseband precoding matrix per subcarrier, $\mathbf{P}_{\text{RF}} \in \mathbb{C}^{\mathcal{Q}^{(r)} \bar{\mathcal{Q}}^{(r)} \times \mathcal{Q}^{(t)}}$ is the analog RF beamforming matrix, and $\mathbf{s}[m] = [s_1, s_2, \dots, s_{N_{\text{tot}}}]^T \in \mathcal{X}^{N_{\text{tot}} \times 1}$ is the information-bearing symbol vector consisting of data symbols drawn from a quadrature amplitude modulation (QAM) constellation, \mathcal{X} . We assume normalized symbols, $\mathbb{E}(\mathbf{s}[m] \mathbf{s}^*[m]) = \frac{P_t}{MN_{\text{tot}}} \mathbf{I}_{N_{\text{tot}}}$, where P_t is the average total Tx power over M -subcarriers. We adopt this model for simulating THz-specific beam-split effects. For other scenarios, the system model reduces to a single-input single-output (SISO) model. We adapt the TeraMIMO THz channel simulator [52] to account for diverse scenarios.

III. SC/MC WAVEFORMS: KEY PERFORMANCE INDICATORS AND ANALYSIS

Choosing a suitable waveform is a challenging task that depends on several conflicting communication system performance requirements and design criteria. For fairness of comparison, we consider the transmission of $M \times N$ complex symbols of bandwidth $B = M\Delta f$, with SCS Δf and frame duration $T_f = NT$, for both SC and MC schemes; the signal period (T) differs between waveforms. We discretize the time-frequency (TF) domain into a lattice, Λ , by sampling time and frequency at integer multiples of T and Δf , respectively.

$$\Lambda = \{(nT, m\Delta f), n=0, \dots, N-1, m=0, \dots, M-1\}. \quad (4)$$

Similarly, we discretize the delay-Doppler (DD) plane into

$$\Lambda^\perp = \left\{ \left(\frac{k}{NT}, \frac{l}{M\Delta f} \right), k=0, \dots, N-1, l=0, \dots, M-1 \right\}, \quad (5)$$

where $\frac{1}{NT}, \frac{1}{M\Delta f}$ define the Doppler and delay domain resolutions, respectively. The maximum supported Doppler and delay spreads are $\nu_{\text{max}} = \frac{v}{c} f_c < 1/T$ and $\tau_{\text{max}} < 1/\Delta f$, respectively, where v is the user velocity, c is the speed of light, and f_c is the carrier frequency.

Both TF and DD lattices are shown in Fig. 2, where we denote by \mathbf{D}_{TF} and $\mathbf{D}_{\text{DD}} \in \mathbb{C}^{M \times N}$ the data symbol matrices (of elements $d_{\text{TF}}[m, n]$ and $d_{\text{DD}}[l, k]$) in the TF and DD

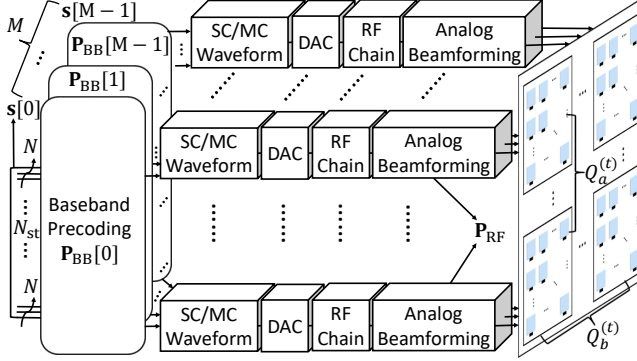


Fig. 1: Block diagram of a THz-band UM-MIMO transmitter.

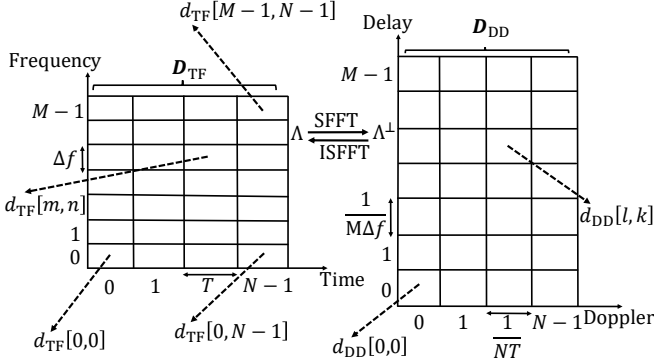


Fig. 2: Illustration of time-frequency delay-Doppler lattices.

domains, respectively. In vector form, $\mathbf{d}_{\text{TF}} = \text{vec}(\mathbf{D}_{\text{TF}})$ and $\mathbf{d}_{\text{DD}} = \text{vec}(\mathbf{D}_{\text{DD}})$. Furthermore, $\mathbf{d}_M^{\text{TF}} \in \mathbb{C}^{M \times 1}$ is a column of \mathbf{D}_{TF} (of elements $d_{\text{TF}}[m]$). In the case of DFT-s-OFDM, the data symbol matrix is $\bar{\mathbf{D}}_{\text{TF}} \in \mathbb{C}^{\bar{M} \times \bar{N}}$, a sub-matrix of \mathbf{D}_{TF} , where \bar{M} represents the number of Tx symbols modulated over M subcarriers. We also denote by $\bar{\mathbf{d}}_{\bar{M}}^{\text{TF}} \in \mathbb{C}^{\bar{M} \times 1}$ a column of $\bar{\mathbf{D}}_{\text{TF}}$. Moreover, for DFT-s-OTFS, the data matrix is $\bar{\mathbf{D}}_{\bar{N}M} \in \mathbb{C}^{\bar{M} \times \bar{N}}$, where $\bar{N}M$ represents the number of Tx symbols. Note that $\mathbf{S} = [\mathbf{s}[0], \mathbf{s}[1], \dots, \mathbf{s}[M-1]]$ of (3), for a single data stream ($N_{\text{st}} = 1$; no digital baseband precoding), reduces to $\mathbf{D}_{\text{TF}}^{\text{T}}$.

The general form of a continuous-time MC modulator, $x(t)$, can be expressed using the discrete Heisenberg transform [42], parameterized by a pulse-shaping prototype filter, $g_{\text{tx}}(t)$, as

$$x(t) = \sum_{m=0}^{M-1} \sum_{n=0}^{N-1} d_{\text{TF}}[m, n] g_{m,n}(t), \quad (6)$$

$$g_{m,n}(t) = g_{\text{tx}}(t - nT) e^{j2\pi m \Delta f (t - nT)}, \quad (7)$$

where $d_{\text{TF}}[m, n]$ represents the Tx symbol at subcarrier-index m and time-index n . The complex orthogonality condition for the basis pulse $g_{m,n}(t)$ is expressed as $\langle g_{m_1, n_1}(t), g_{m_2, n_2}(t) \rangle = \delta_{(m_2-m_1), (n_2-n_1)}$, with δ being the Kronecker delta function. The discrete-time representation of (6) (Nyquist sampling at $F_s = \frac{1}{T_s} = B$; limited by ADC/DAC specifications) is

$$x[uT_s] = \sum_{m=0}^{M-1} \sum_{n=0}^{N-1} d_{\text{TF}}[m, n] g_{m,n}[uT_s], \quad (8)$$

where $u = \{0, 1, \dots, MN-1\}$. The PAPR of a discrete-time signal $x[u]$ over a finite observation period N_{per} is expressed

as a random variable [59]

$$\text{PAPR}(x[u]) = \max_{u \in [0, N_{\text{per}}-1]} \left(|x[u]|^2 \right) / \mathbb{E} \left(|x[u]|^2 \right), \quad (9)$$

the statistical behavior of which can be estimated through numerical simulations. However, the PAPR for the discrete-time baseband signal, $x[u]$, is noticeably lower than the PAPR of the continuous-time baseband signal, $x(t)$. Thus, we perform L -times interpolation (oversampling), where $L \geq 4$, to obtain a close PAPR to that of $x(t)$. We characterize the complementary cumulative distribution function (CCDF) of PAPR. In the remainder of this section, we detail various KPIs and introduce several schemes, namely, CP-OFDM, DFT-s-OFDM, SC-FDE, OQAM/FBMC, OTFS, and DFT-s-OTFS, as illustrated in Fig. 3.

A. Spectral Efficiency and Physical Layer End-to-End Latency

The SE (bits/sec/Hz) is an essential indicator of throughput and achievable rate for a given bandwidth. Since the THz band promises huge available bandwidths, unlike below 6 GHz communications, SE is not a primary concern. However, SE is still important for data demanding use cases, such as THz-enabled holographic video meeting, augmented reality (AR), and virtual reality (VR). Similarly, the PH-E2E latency, which is the delay between information transmission (bits at the output of the channel encoder) and recovery (bits at the input of the channel decoder), is waveform-dependant (overlapping in OQAM/FBMC lengthens the frame duration, for example). Nevertheless, the ultra-broadband THz bandwidth (B) ensures a very small sampling period (T_s). The processing time of the equalizer and channel encoder/decoder (not included in our PH-E2E latency definition) are more critical at THz frequencies and are also dependent on the used waveform.

B. Power Spectral Density and Out-of-Band Emissions

The power spectral density (PSD) and OOB emissions follow strict standard regulations to meet spectrum mask requirements. For example, the international telecommunications union (ITU) radio regulation 5.340 prohibits transmissions in ten passive bands over 100 – 252 GHz to protect deep space observatories and satellite sensors [60], resulting in a maximum available contiguous bandwidth of 23 GHz. OOB emissions are also critical in integrated space-air-ground THz networks. It is thus important to study OOB-induced interference to neighboring systems and among multiple users, highlighting the role of carrier-aggregation techniques. The severity of OOB emissions is dictated by bandwidth, required SE, and neighboring co-operating systems. The waveform Tx spectrums in the IEEE 802.15.3d sub-THz standard are described for different bandwidths in [17].

C. Transceiver Complexity

The computational complexity of the studied SC/MC transceivers is arguably the most important KPI to consider, given the limited processing capabilities at Tbps and the need for low-cost and low-power solutions. Without loss of generality, we only consider the number of real multiplications per

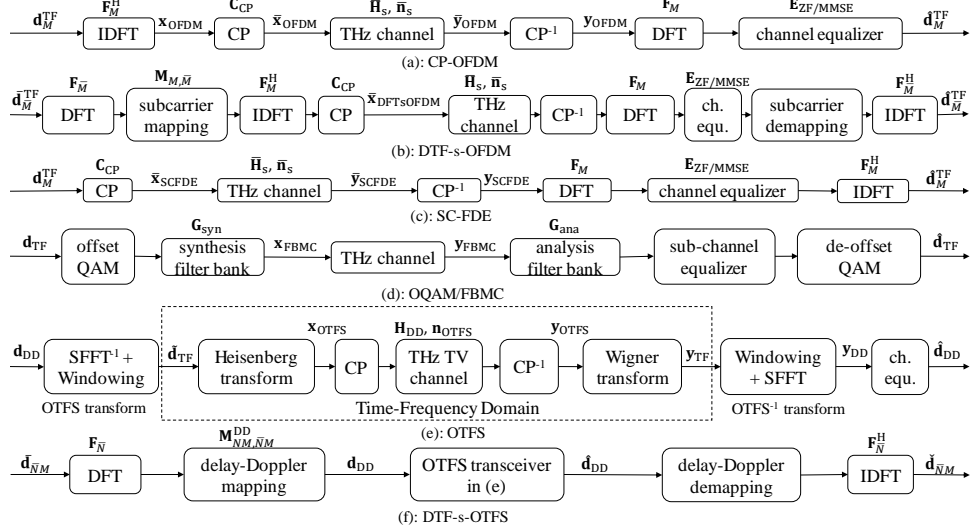


Fig. 3: SC/MC transceiver block diagrams: (a) CP-OFDM, (b) DFT-s-OFDM, (c) SC-FDE, (d) OQAM/FBMC, (e) OTFS, and (f) DFT-s-OTFS

unit of time in the modulation, demodulation, and equalization processes. The complexity of channel coding and decoding are important in their own right but not included in our study.

The number of real multiplications in an M -point fast Fourier transform (FFT)/inverse FFT (IFFT) (split-radix algorithm) is [61]

$$\bar{C}_{\text{FFT}}(M) = M(\log_2(M) - 3) + 4. \quad (10)$$

As illustrated in Fig. 3(a), IFFT/FFT is followed by rectangular pulse-shaping in CP-OFDM, resulting in a complexity (\bar{C}_{OFDM}) and number of multiplications per unit time (C_{OFDM}):

$$\begin{aligned} \bar{C}_{\text{OFDM}}^{(t)/(r)} &= \bar{C}_{\text{FFT}}(M) + 4(M+N_{\text{CP}}), \bar{C}_{\text{OFDM}}^{(\text{eq})} = 4M, \\ C_{\text{OFDM}} &= \frac{N(\bar{C}_{\text{OFDM}}^{(t)/(r)} + \bar{C}_{\text{OFDM}}^{(\text{eq})})}{N(M+N_{\text{CP}})T_s} = \frac{\bar{C}_{\text{OFDM}}^{(t)/(r)} + \bar{C}_{\text{OFDM}}^{(\text{eq})}}{M+N_{\text{CP}}} F_s. \end{aligned} \quad (11)$$

Furthermore, in the case of DFT-s-OFDM (Fig. 3(b)), the equalization complexity remains the same, while an additional precoding FFT/IFFT block in Tx/Rx results in

$$\begin{aligned} \bar{C}_{\text{DFTsOFDM}}^{(t)/(r)} &= \bar{C}_{\text{FFT}}(M) + \bar{C}_{\text{FFT}}(\bar{M}) + 4(M+N_{\text{CP}}), \\ C_{\text{DFTsOFDM}}^{(t)/(r)} &= \frac{\bar{C}_{\text{DFTsOFDM}}^{(t)/(r)} + \bar{C}_{\text{DFTsOFDM}}^{(\text{eq})}}{M+N_{\text{CP}}} F_s. \end{aligned} \quad (12)$$

SC-FDE enjoys relatively low Tx complexity as symbols are directly transmitted after CP (Fig. 3(c)). However, with FFT/IFFT at Rx, the overall transceiver complexity is that of CP-OFDM (complexity shift from Tx to Rx); $\bar{C}_{\text{OFDM}} = \bar{C}_{\text{SCFDE}}$. For OQAM/FBMC, we consider the direct form polyphase prototype filter realization, with a filter length of $L_p = O \times M$ (O is the pulse-shaping overlapping factor). In general, a multi-tap channel equalization per subcarrier with an equalizer of length L_{eq} is used for this waveform. Accounting for OQAM, phase offsets (for linear phase filters), IFFT, filtering, 50% overlapping, and equalization, \bar{C}_{FBMC} , and C_{FBMC} add up

to [32]

$$\begin{aligned} \bar{C}_{\text{FBMC}}^{(t)/(r)} &= 2\bar{C}_{\text{FFT}}(M) + 4L_p + 4M, \bar{C}_{\text{FBMC}}^{(\text{eq})} = 4ML_{\text{eq}}, \\ C_{\text{FBMC}} &= \frac{N(\bar{C}_{\text{FBMC}}^{(t)/(r)} + \bar{C}_{\text{FBMC}}^{(\text{eq})})}{M(N+O-1/2)} F_s, \end{aligned} \quad (13)$$

where the first multiplication by a factor of 2 accounts for complex-valued QAM symbols that are separated into two real-valued symbols. The OQAM/FBMC complexity is slightly dependant on (O). Note that we only assume a one-tap equalizer in simulations ($L_{\text{eq}} = 1$). OQAM/FBMC is clearly more complex than CP-OFDM. While for OTFS¹, based on (42), the complexity and number of multiplications per unit time are expressed as

$$\begin{aligned} \bar{C}_{\text{OTFS}}^{(t)/(r)} &= \bar{C}_{\text{FFT}}(N) + 4(N+N_{\text{CP}}/M), \bar{C}_{\text{OTFS}}^{(\text{eq})} = O(M^3N^3), \\ C_{\text{OTFS}}^{(t)/(r)} &= \frac{M\bar{C}_{\text{OTFS}}^{(t)/(r)} + \bar{C}_{\text{OTFS}}^{(\text{eq})}}{NM+N_{\text{CP}}} F_s. \end{aligned} \quad (14)$$

Hence, $\bar{C}_{\text{OTFS}}/C_{\text{OTFS}}$ are functions of both N and M^2 . Moreover, in the case of DFT-s-OTFS (Fig. 3(f)), following the same logic of DFT-s-OFDM:

$$\begin{aligned} \bar{C}_{\text{DFTsOTFS}}^{(t)/(r)} &= \bar{C}_{\text{OTFS}}^{(t)/(r)} + \bar{C}_{\text{FFT}}(\bar{N}), \bar{C}_{\text{DFTsOTFS}}^{(\text{eq})} = O(M^3N^3), \\ C_{\text{DFTsOTFS}}^{(t)/(r)} &= \frac{M\bar{C}_{\text{DFTsOTFS}}^{(t)/(r)} + \bar{C}_{\text{DFTsOTFS}}^{(\text{eq})}}{NM+N_{\text{CP}}} F_s. \end{aligned} \quad (15)$$

From (14) and (15), we note that the complexities of OTFS

¹In this work, we use OTFS with rectangular Tx and Rx windowing and pulse-shaping, and consider one CP per frame ($M \times N$ symbols), which results in a low-complexity implementation [62]. This setting is different from the OTFS setting in [42] with complexity $\bar{C}_{\text{OTFS}}^{(t)/(r)} = 2\bar{C}_{\text{FFT}}(M) + \bar{C}_{\text{FFT}}(N) + 4(N+N_{\text{CP}}/M)$ and the OFDM-based OTFS setting in [44] which adds one CP every N blocks (each block is of length M). See Sec. III-K for more details.

²In this work, we adopt the classical linear equalizer for OTFS. However, low-complexity iterative and non-iterative solutions can be used. See Table 2 in [63] for an extended comparison of complexity costs.

and DFT-s-OTFS are dominated by DD equalization.

D. Peak to Average Power Ratio

PAPR is an essential and important KPI for sub-THz/THz communications as it dictates the Tx power efficiency, which affects energy efficiency, link budget, and coverage (processing ultra-wide bandwidth sub-THz/THz signals is very power consuming). Large amplitude fluctuations in high PAPR lead to spectral regrowth and non-linear distortion; an output back-off is thus needed to retain the linear PA region, reducing power efficiency. The saturated output power (P_{sat}) recordings in state-of-the-art THz PAs [29] reveal limited achievable output power that decreases drastically with operating frequency (the trend lines for different technologies follow a stepper increasing-slope). For example, $P_{\text{sat}} \approx 20, 23 \text{ dBm}$ and 28 dBm at $f_c = 100 \text{ GHz}$ for CMOS, SiGe BiCMOS, and InP technologies, respectively. Furthermore, high PAPR necessitates high dynamic-range THz ADCs of low signal-to-quantization-noise ratios, which are not cost- and power-efficient [64]. The ADC signal-to-noise and distortion ratio (SNDR) decreases by increasing the Nyquist sampling rate. However, the energy per conversion step increases linearly with frequency beyond 100 MHz [65]. For example, for an ADC of $F_s = 100 \text{ GHz}$, the power consumption and SNDR are approximately 0.3 Watt (very high) and 35 dB (very low), respectively. The PAPR CCDF of one CP-OFDM symbol ($N=1$) is expressed as [59]

$$\Pr(\text{PAPR}(x_{\text{OFDM}}) > \gamma_{\text{th}}) = 1 - (1 - e^{-\gamma_{\text{th}}})^M, \quad (16)$$

for a PAPR threshold γ_{th} . Furthermore, the closed-form approximation of the PAPR CCDF of OQAM/FBMC in [59] reveals higher PAPR values compared to CP-OFDM due to per-subcarrier filtering. In [66], the PAPR CCDF of discrete-time OTFS (no oversampling and rectangular pulse-shaping) is approximated for high values of N as

$$\Pr(\text{PAPR}(x_{\text{OTFS}}) > \gamma_{\text{th}}) \approx 1 - (1 - e^{-\gamma_{\text{th}}})^{MN}. \quad (17)$$

The work in [66] shows that the PAPR CCDF of OTFS increases with M as the probability of having large peaks increases. However, the maximum OTFS PAPR is upper-bounded by a linear function of N [66], unlike TF MC modulations, such as OFDM, where the PAPR grows linearly with the number of subcarriers M . Note that generalizing (16) over the entire frame approximates (17); OTFS provides significantly better PAPR than OFDM for ($N < M$). Thus, OTFS PAPR is not energy-efficient for THz system design. This problem is solved by using a DFT spreading block with OTFS in the uplink [46], where the PAPR upper bound grows linearly with the DFT spreading size \bar{N} . Since \bar{N} is less than the number of the OTFS symbols in a frame (N) and the number of subcarriers (M) in a wideband THz channel, ($\bar{N} < N < M$), we expect that DFT-s-OTFS can achieve lower PAPR than both OTFS and OFDM. Thus, DFT-OTFS promises to be a more energy-efficient solution for future THz communications. Furthermore, other SCs inherently result in low PAPR, whether in SC-FDE or DFT-s-OFDM, due to DFT precoding.

E. Robustness to Hardware Impairments

THz-band transceivers are substantially more vulnerable to conventional RF impairments than microwave and mmWave transceivers. Therefore, the following KPIs are crucial to mitigate the corresponding impairments in the design process.

1) *Phase Noise*: Due to time-domain instability, the local oscillator (LO) output can be a phase-modulated tone. PHN in THz devices (that are not yet mature) has more severe consequences than in microwave or mmWave devices. The motivation to use low-cost devices for THz communications is also limiting, where achieving low PHN requires advanced complex techniques such as phase-locked loops [67]. In particular, if the THz LO signal is generated using a low-cost low-frequency oscillator followed by frequency multipliers, the required multiplication factor, ξ , is relatively high, which further increases the PHN power by a factor of ξ^2 . Therefore, PHN increases by 6 dB for every doubling of the oscillation frequency [67]. Furthermore, PHN causes significant performance degradation and reduces the effective signal-to-interference plus noise ratio (SINR) at the Rx, limiting both data rate and BER. Note that increasing the signal-to-noise ratio (SNR) does not mitigate the PHN effects. Therefore, optimized SC schemes and non-coherent modulations that are inherently robust to PHN are argued to be good candidates for sub-THz communications [20].

There are several approaches for modeling PHN, two of which are most prominent. The first is a correlated model that uses the superposition of Wiener (Gaussian random-walk) and Gaussian processes; the second is an uncorrelated model that considers only a Gaussian noise reflecting the white PHN floor. The appropriate choice of PHN models for sub-THz band is addressed in [50], where it is argued that the uncorrelated Gaussian PHN model should be favored if the system bandwidth (B) is large enough compared to the oscillator corner frequency (f_{cor}):

$$N \left(\frac{f_{\text{cor}}}{B} \right)^2 \leq \frac{\ln(2)}{2\pi}. \quad (18)$$

Therefore, the Rx signal, at instant u , is expressed as

$$y[u] = \left(h[u] * \left(x[u] e^{j\phi^{(t)}[u]} \right) \right) e^{j\phi^{(r)}[u]} + n[u], \quad (19)$$

where $*$ denotes linear convolution, and $\phi^{(t)}[u], \phi^{(r)}[u]$ are discrete stochastic processes representing Tx, Rx LO PHN, respectively. The correlated model is defined as

$$\phi[u] = \phi_w[u] + \phi_g[u], \quad (20)$$

where the Wiener and Gaussian PHN models are expressed, respectively, as

$$\phi_w[u] = \phi_w[u-1] + \theta_w[u], \quad \theta_w[u] \sim \mathcal{N}(0, \sigma_w^2), \quad (21)$$

$$\phi_g[u] \sim \mathcal{N}(0, \sigma_g^2). \quad (22)$$

The uncorrelated PHN implies $\phi[u] = \phi_g[u]$. The variances are defined as $\sigma_w^2 = 4\pi^2 K_2 T$ and $\sigma_g^2 = K_0 / T$, where K_0 and K_2 are the PHN levels that can be evaluated from the measured PHN PSD, the corner frequency is ($f_{\text{cor}} = K_2 / K_0$), $T = 1/B$ is the modulated signal duration, and B is the system bandwidth [68]

(a strong dependence of system performance on bandwidth).

2) *Wideband IQI*: The frequency-dependent wideband IQI is another dominant hardware impairment in THz transceivers operating over ultra-wide bandwidths. Efficient signal processing techniques have been extensively studied for narrowband IQI at both Tx (via digital pre-distortion) and Rx. However, only a few works address the wideband IQI model in the THz-band, such as [48] for SC-FDE. Furthermore, wideband PA non-linearity models still lack in the THz literature. Extensive research to study such impairments is crucial. However, the existing models for wideband systems operating at 60 GHz [69] can be used to provide a preliminary analysis and evaluation of THz candidates.

F. Robustness to THz-specific Impairments

THz-specific channel-induced impairments should also be considered when studying candidate waveforms. For example, THz propagation suffers from misalignment between Tx and Rx, which is highly probable given the narrow THz beams [52]. Another THz channel characteristic is the spherical wave propagation model (SWM), which should be accounted for at relatively short communication distances [52]. More importantly, a beam split effect arises in wideband UM-MIMO beamforming. In particular, the difference between the carrier and center frequencies, f_m and f_c , results in THz path components squinting into different spatial directions at different subcarriers, causing severe array gain loss [52]. Such beam split is mainly caused by frequency-independent delays in analog-beamforming PSs. Furthermore, large UM-MIMO THz arrays result in very narrow beamwidths that worsen this effect. Several beam-split mitigation methods are proposed in the literature, such as delay-phase precoding in [70], where CP-OFDM is assumed. However, the effect of beam split on other SC/MC schemes is not yet studied. This work only studies the impairment caused by beam split as it is more relevant to waveform design than misalignment and SWM.

G. CP-OFDM

The discrete-time Tx OFDM signal is derived from (8) ($N = 1$) using rectangular pulse-shaping:

$$x_{\text{OFDM}}[u] = \sum_{m=0}^{M-1} d_{\text{TF}}[m] g_{\text{tx}}[u] e^{j2\pi \frac{m}{M} u},$$

$$g_{\text{tx}}[u] = \begin{cases} \frac{1}{\sqrt{M}} & u = 0, \dots, M-1 \\ 0 & \text{otherwise,} \end{cases} \quad (23)$$

$$\mathbf{x}_{\text{OFDM}} = \mathbf{F}_M^H \mathbf{d}_M^{\text{TF}}. \quad (24)$$

To combat inter-symbol interference (ISI) in a time-dispersive wireless channel of length $N_{\text{ch}} = \tau_{\text{rms}}/T_s$, where τ_{rms} is the root mean square (RMS) delay spread, a guard interval of $N_{\text{CP}} \geq N_{\text{ch}}$ samples is added to the Tx signal. The CP-OFDM signal can thus be expressed as

$$\bar{\mathbf{x}}_{\text{OFDM}} = \mathbf{C}_{\text{CP}} \mathbf{x}_{\text{OFDM}}; \quad \mathbf{C}_{\text{CP}} = \begin{bmatrix} \mathbf{0}_{N_{\text{CP}}, M-N_{\text{CP}}} & \mathbf{I}_{N_{\text{CP}}} \\ \mathbf{I}_M & \end{bmatrix}. \quad (25)$$

where $\bar{\mathbf{x}}_{\text{OFDM}} = [x_{\text{OFDM}}[-N_{\text{CP}}], \dots, x_{\text{OFDM}}[0], \dots, x_{\text{OFDM}}[M-1]]^T$, and \mathbf{C}_{CP} is the CP-insertion matrix of size $M_t \times M$, $M_t = M + N_{\text{CP}}$, defined as The total CP-OFDM symbol duration, $T = (M + N_{\text{CP}})T_s = T_u + T_{\text{CP}}$, is that of the CP duration (T_{CP}) plus the useful symbol duration (T_u). Although CP reduces SE (Table IV), it emulates a cyclic convolution with the channel, allowing simple FDE through FFT. The received signal over a SISO channel of impulse response $\mathbf{h}_s = [h_0, \dots, h_{N_{\text{ch}}-1}]^T$, after CP removal is

$$\mathbf{y}_{\text{OFDM}} = \mathbf{H}_s \mathbf{x}_{\text{OFDM}} + \mathbf{n}_s, \quad (26)$$

where assuming perfect time and frequency synchronization, \mathbf{H}_s is an $M \times M$ circular convolution matrix of band-diagonal structure built upon \mathbf{h}_s , and $\mathbf{n}_s \sim \mathcal{CN}(\mathbf{0}, \sigma_n^2 \mathbf{I}_M)$ is the AWGN vector. Note that the actual transmission is expressed as $\bar{\mathbf{y}}_{\text{OFDM}} = \bar{\mathbf{H}}_s \bar{\mathbf{x}}_{\text{OFDM}} + \bar{\mathbf{n}}_s$, where $\bar{\mathbf{H}}_s \in \mathbb{C}^{(M+N_{\text{ch}}-1) \times M_t}$ is derived from \mathbf{H}_s , and $\bar{\mathbf{n}}_s \sim \mathcal{CN}(\mathbf{0}, \sigma_n^2 \mathbf{I}_{M+N_{\text{ch}}-1})$. The signal is then processed by a DFT block \mathbf{F}_M . Equalization can be performed using zero-forcing (ZF) or minimum mean-squared error (MMSE), with corresponding equalization matrices

$$\mathbf{E}_{\text{ZF}} = (\mathbf{H}_s^H \mathbf{H}_s)^{-1} \mathbf{H}_s^H, \quad (27)$$

$$\mathbf{E}_{\text{MMSE}} = (\mathbf{H}_s^H \mathbf{H}_s + \frac{\sigma_n^2}{P_x} \mathbf{I}_M)^{-1} \mathbf{H}_s^H,$$

where P_x is the signal power. The Tx symbol estimates are retrieved as $\hat{\mathbf{d}}_M^{\text{TF}} = J(\mathbf{E} \mathbf{F}_M \mathbf{y}_{\text{OFDM}})$, where $J(\cdot)$ maps an equalized symbol to the closest symbol in \mathcal{X} . Note that (24) can be generalized to express the Tx CP-OFDM frame (N symbols) as

$$\bar{\mathbf{X}}_{\text{OFDM}} = \mathbf{C}_{\text{CP}} \mathbf{F}_M^H \mathbf{D}_{\text{TF}}, \quad (28)$$

$$\mathbf{x}_{M,N}^{\text{OFDM}} = \text{vec}(\bar{\mathbf{X}}_{\text{OFDM}}) = (\mathbf{I}_N \otimes \mathbf{C}_{\text{CP}}) \left(\mathbf{I}_N \otimes \mathbf{F}_M^H \right) \mathbf{d}_{\text{TF}}.$$

Designing a CP-OFDM system requires tuning many parameters such as the number of subcarriers (M), the CP duration (T_{CP}), and the SCS (Δf). Such parameters are chosen such that

$$\tau_{\text{rms}} \leq T_{\text{CP}} \leq T_u \ll T_{\text{coh}}; \quad \Delta f = \frac{1}{T_u} = \frac{B}{M}, \quad (29)$$

where $B_{\text{coh}} = \frac{1}{5\tau_{\text{rms}}}$ is the coherence bandwidth and $T_{\text{coh}} = \sqrt{\frac{9}{16\pi\nu_{\text{max}}} \times \frac{1}{\nu_{\text{max}}}}$ is the coherence time. The SCS satisfies (29) to ensure orthogonality and maximize SE.

The SCS choice also affects PH-E2E latency, PAPR, complexity, and equalization performance. In particular, the SCS provides a trade-off between CP overhead, sensitivity to Doppler spread, and robustness to hardware imperfections. The CP length is also a critical design parameter, where larger N_{CP} relaxes time synchronization constraints caused by STO, but also at the expense of larger CP overhead (decreased SE). Furthermore, the number of subcarriers (M) impacts the PAPR performance (16) and the FFT/IFFT complexity (Sec. III-C).

The transmission spectra and molecular absorption dictate the large available bandwidth in THz LoS scenarios [52]. However, in indoor THz scenarios, the channel can be LoS-dominant and non-LoS (NLoS)-assisted, or only NLoS (multi-path). Based on the coherence bandwidth, for a given com-

munication distance, we decide on the corresponding design parameters of a frequency-flat channel or FSC per subcarrier. For example, for a communication distance of 3 m, in the sub-THz band ($f_c = 0.3$ THz), $B_{coh} = 1$ GHz; in the THz band ($f_c = 0.9$ THz), $B_{coh} \approx 5$ GHz [16].

We list in Table I some of the expected CP-OFDM parameters for sub-THz/THz band communications, alongside parameters adopted in both 4G-LTE (below 6 GHz) and 5G-NR (below 6 GHz and mmWaves). In a nutshell, CP-OFDM enjoys a relatively low-complexity implementation (using FFT), is robust to multi-path fading, and uses a simple FDE method (single-tap equalizer for a broadband FSC). However, the resultant high PAPR is challenging for power-limited sub-THz/THz communications. Moreover, the CP-OFDM time tolerance for symbol synchronization is very low (order of nanoseconds) due to the expected small T_{CP} and τ_{rms} .

H. DFT-s-OFDM

DFT-s-OFDM, also known as precoded OFDM, is adopted in 4G-LTE/5G-NR uplink and is a promising candidate for THz communications. The use of a DFT-block at the Tx reduces the PAPR and retains all SC benefits, albeit at a marginal complexity cost. DFT-s-OFDM thus aims at reducing power consumption and PA costs at user terminal. When data symbol blocks are assigned to different users, DFT-s-OFDM reduces to SC-FDMA in multi-user scenarios.

As illustrated in Fig. 3(b), data symbols are first spread in DFT-precoding; the outputs are the complex symbols that modulate the OFDM subcarriers. For a selection of $\bar{M} \leq M$ subcarriers to be modulated. The Tx signal is expressed as

$$\bar{\mathbf{x}}_{DFTsOFDM} = \mathbf{C}_{CP} \mathbf{F}_M^H \left(\mathbf{M}_{M, \bar{M}} \mathbf{F}_{\bar{M}} \bar{\mathbf{d}}_{\bar{M}}^{\text{TF}} \right), \quad (30)$$

where $\mathbf{M}_{M, \bar{M}}$ is a mapping matrix between data symbols and the \bar{M} active subcarriers (zero insertion at $M - \bar{M}$ unused subcarriers). The mapping can be localized or distributed. In the localized mode, $\mathbf{M}_{M, \bar{M}} = [\mathbf{I}_{\bar{M}}, \mathbf{0}_{\bar{M}, M - \bar{M}}]^T$, and the DFT outputs are directly mapped to a subset of consecutive subcarriers. In the distributed mode, the DFT outputs are assigned to non-continuous subcarriers over the entire bandwidth. The additional need for signaling, pilots, and guard bands (in multiple access scenarios) in the distributed mode increases the system complexity, whereas the straightforward implementation of equal SCS in the localized mode is favorable.

I. SC-FDE

A promising alternative to CP-OFDM is SC-FDE, which combines the benefits of CP and FDE, and has low PAPR due to low envelope variations. Unlike in CP-OFDM, where each data symbol is allocated a small bandwidth over a long symbol duration, in SC-FDE, data symbols are assigned to a single large bandwidth with short symbol durations. For the same CP-OFDM symbol duration, the SC-FDE Tx signal, containing M symbols, can be expressed as

$$\bar{\mathbf{x}}_{SCFDE} = \mathbf{C}_{CP} \left(\mathbf{F}_M^H \mathbf{F}_M \right) \mathbf{d}_M^{\text{TF}} = \mathbf{C}_{CP} \mathbf{d}_M^{\text{TF}}. \quad (31)$$

The remainder transmission, equalization, and demodulation stages are similar to those of CP-OFDM, as shown in Fig. 3(c).

The SC-FDE synchronization algorithms are also very similar to those of CP-OFDM. Furthermore, the spectral shape of the SC-FDE waveform is determined by the Tx pulse-shaping, used DAC, and RF filtering stages. It is worth noting that the choice of pulse-shaping affects the PAPR, OOB emissions, complexity, and immunity to hardware impairments.

J. OQAM/FBMC

OQAM/FBMC is another promising waveform candidate, especially for cognitive radio (CR) and dynamic/intelligent spectrum sharing applications. OQAM/FBMC offers high SE (no need for CP), low OOB levels, and low sensitivity to CFO. Furthermore, by using a per-subcarrier well-localized pulse-shaping filter in both time and frequency (such as PHYDYAS [71]), OQAM/FBMC supports enhanced synchronization procedures. However, such benefits come at the cost of limited integration with MIMO systems (maintaining real orthogonality in OQAM complicates precoder design [72]), higher PAPR compared to OFDM (due to subcarrier filtering), and higher complexity (especially in the equalizer as there is no CP). Given the importance of such KPIs at high frequencies, OQAM/FBMC is not a good candidate for THz communications.

The direct form of an OQAM/FBMC system is illustrated in Fig. 3(d), consisting of OQAM pre-processing, a synthesis filter bank (SFB), an analysis filter bank (AFB), and OQAM post-processing. We assume a low-complexity implementation based on a polyphase filter structure (PHYDYAS with overlapping factor O) and FFT, as described in [71] (Figures (2-7) and (2-8)). OQAM/FBMC satisfies the real orthogonality condition, $\mathcal{R}(\langle g_{m_1, n_1}^{\text{FBMC}}(t), g_{m_2, n_2}^{\text{FBMC}}(t) \rangle) = \delta_{(m_2 - m_1), (n_2 - n_1)}$, instead of complex orthogonality. Thus, the useful symbol time still satisfies $\Delta f = 1/T_u$, but the symbol duration is $T = T_u/2$. The Tx signal can be derived from (6) by adding to the Tx basis pulse in (7) a phase shift, $\beta_{m, n} = \frac{\pi}{2}(m+n)$:

$$g_{m, n}^{\text{FBMC}}(t) = g_{tx}^{\text{FBMC}}(t - nT) e^{j2\pi m \Delta f (t - nT)} e^{j\beta_{m, n}}. \quad (32)$$

Such a phase shift transfers the induced interference between symbols to the imaginary domain [73]. The resultant basis pulse in (32) is a frequency- and time-shifted version of the prototype filter $g_{tx}^{\text{FBMC}}(t)$. Furthermore, the prototype filter is designed using the frequency-sampling technique, with $(2O-1)$ non-zero frequency-domain samples for an overlapping factor O . For filter of length L_p and coefficients $\psi[o]$'s (defined in [71]), the impulse response is

$$g_{tx}^{\text{FBMC}}[i] = 1 + 2 \sum_{o=1}^{O-1} (-1)^o \psi[o] \cos \left(\frac{2\pi o}{L_p} (i+1) \right). \quad (33)$$

Then, the discrete-time Tx signal can be express as

$$\mathbf{x}_{FBMC} = \mathbf{G}_{\text{syn}} \mathbf{d}_{\text{TF}}, \quad (34)$$

where the time interval is $-OT_u/2 \leq t < OT_u/2 + (N-1)T$ and $\mathbf{G}_{\text{syn}} \in \mathbb{C}^{N_t \times MN}$ is the Tx matrix that contains the basis pulse-shaping vectors $\mathbf{g}_{m, n}^{\text{FBMC}} \in \mathbb{C}^{N_t \times 1}$ ($N_t = (OT_u + (N-1)T) F_s$), defined as

$$\mathbf{G}_{\text{syn}} = [\mathbf{g}_{0,0}^{\text{FBMC}} \ \dots \ \mathbf{g}_{M-1,0}^{\text{FBMC}} \ \mathbf{g}_{0,1}^{\text{FBMC}} \ \dots \ \mathbf{g}_{M-1,N-1}^{\text{FBMC}}], \quad (35)$$

TABLE I: Key parameters for CP-OFDM at different bands

Parameter \ Band	below 6 GHz	mmWave	sub-THz	THz
SCS - Δf (KHz)	$2^\mu \times 15, \mu = 0$ (4G-LTE) $2^\mu \times 15, \mu = 0, 1, 2$ (5G-NR)	$2^\mu \times 15, \mu = 2, 3, 4$	$2^\mu \times 5000, \mu = 0, 1$	$2^\mu \times 25000, \mu = 0, 1$
System bandwidth - B (MHz)	1.25 up to 20 (4G-LTE) 5 up to 100 (5G-NR)	50, 100, 200, 400	$[10-20] \times 10^3$	$[20-100] \times 10^3$
Number of subcarriers - M	128 up to 2048 (4G-LTE) up to 4096 (5G-NR)	up to 4096	up to 2048	up to 2048
Number of used subcarriers	76 up to 1200 (4G-LTE) up to 3300 (5G-NR)	up to 3300	up to 1200	up to 1200

$$\mathbf{g}_{m,n}^{\text{FBMC}}[n_t] = g_{m,n}^{\text{FBMC}}(t)|_{t=n_t T_s - \frac{\sigma_{T_s}}{2}}, n_t = 0, 1, \dots, N_t. \quad (36)$$

At the Rx, the analysis filter, $\mathbf{G}_{\text{ana}} = \mathbf{G}_{\text{syn}}^H$, is used in matched-filter decoding.

K. OTFS

The recently proposed OTFS waveform [42] is tailored for high-Doppler doubly-selective channels, typically arising in V2X communications. Unlike the other waveforms that modulate data in the TF domain, OTFS modulates data in the DD domain, transforming the TV channel in TF into a 2D quasi-TIV channel in DD. The corresponding transmission frame symbols experience a nearly constant channel gain [74], making OTFS a promising solution in high-Doppler multi-path channels, exploiting the full diversity of TV-FSC and providing substantial delay and Doppler resilience [75]. OTFS is superior to CP-OFDM in this context.

OTFS modulation consists of two main blocks, OTFS transform and Heisenberg transform, as illustrated in Fig. 3(e). Furthermore, OTFS transform involves two stages, inverse symplectic finite Fourier transform (ISFFT) and windowing. ISFFT maps data symbols $d_{\text{DD}}[l, k]$ in the DD domain to samples $d_{\text{TF}}[m, n]$ in the TF domain as follows [74]

$$d_{\text{TF}}[m, n] = \frac{1}{\sqrt{MN}} \sum_{l=0}^{M-1} \sum_{k=0}^{N-1} d_{\text{DD}}[l, k] e^{j2\pi(\frac{nk}{N} - \frac{ml}{M})}. \quad (37)$$

A closer look into (37) reveals that the ISFFT of \mathbf{D}_{DD} is equivalent to an M -point DFT and an N -point IDFT of the columns and rows of \mathbf{D}_{DD} , respectively. Subsequently, (37) can be expressed in matrix and vectorized forms as

$$\mathbf{d}_{\text{TF}} = \mathbf{F}_M \mathbf{D}_{\text{DD}} \mathbf{F}_N^H; \quad \mathbf{d}_{\text{TF}} = (\mathbf{F}_N^H \otimes \mathbf{F}_M) \mathbf{d}_{\text{DD}}. \quad (38)$$

The OTFS transform applies a Tx window $U_{\text{tx}}[m, n]$ to the TF signal in (37). Let $\mathbf{U}_{\text{tx}} = \text{diag}(U_{\text{tx}}[m, n]) \in \mathbb{C}^{MN \times MN}$ and assume rectangular windows for both Tx and Rx ($\mathbf{U}_{\text{tx}} = \mathbf{U}_{\text{rx}} = \mathbf{I}_{MN}$), the OTFS transform output is expressed as

$$\tilde{\mathbf{d}}_{\text{TF}} = \mathbf{U}_{\text{tx}} \mathbf{d}_{\text{TF}}. \quad (39)$$

Heisenberg transform then forms the time-domain Tx signal; combining (6), (7), and (39)

$$x_{\text{OTFS}}(t) = \sum_{m=0}^{M-1} \sum_{n=0}^{N-1} \tilde{d}_{\text{TF}}[m, n] g_{\text{tx}}(t - nT) e^{j2\pi m \Delta f (t - nT)}. \quad (40)$$

The Tx ($g_{\text{tx}}(t)$) and Rx ($g_{\text{rx}}(t)$) pulses ideally satisfy the bi-orthogonality condition [42], although not practical. Let $\mathbf{G}_{\text{tx}} = \text{diag}(g_{\text{tx}}[0], g_{\text{tx}}[T/M], \dots, g_{\text{tx}}[(m-1)T/M]) \in \mathbb{C}^{M \times M}$

be formed from samples of $g_{\text{tx}}(t)$; \mathbf{G}_{rx} similarly defined (assuming rectangular pulse-shaping $\mathbf{G}_{\text{tx}} = \mathbf{G}_{\text{rx}} = \mathbf{I}_M$ [74], then $\tilde{\mathbf{D}}_{\text{TF}} = \mathbf{D}_{\text{TF}}$). We can restructure (40) in matrix and vectorized forms as

$$\mathbf{X}_{\text{OTFS}} = \mathbf{G}_{\text{tx}} \mathbf{F}_M^H \left(\mathbf{F}_M \mathbf{D}_{\text{DD}} \mathbf{F}_N^H \right) = \mathbf{G}_{\text{tx}} \mathbf{D}_{\text{DD}} \mathbf{F}_N^H, \quad (41)$$

$$\mathbf{x}_{\text{OTFS}} = \left(\mathbf{F}_N^H \otimes \mathbf{G}_{\text{tx}} \right) \mathbf{d}_{\text{DD}}. \quad (42)$$

If $g_{\text{tx}}(t)$ is a rectangle pulse-shape of duration T , (40) reduces to IDFT, and for $N=1$, the inner box of Fig. 3(e) is CP-OFDM. Therefore, one OTFS frame is effectively an ISFFT over N consecutive independent OFDM symbols with M subcarriers.

As a spectral-efficient solution, we assume one CP for the entire OTFS frame, of the same duration T_{CP} as in previous waveforms. The Rx signal can be expressed as

$$y_{\text{OTFS}}(t) = \int_{\nu} \int_{\tau} h_{\text{DD}}(\tau, \nu) x_{\text{OTFS}}(t - \tau) e^{j2\pi \nu(t - \tau)} d\tau d\nu + n(t), \quad (43)$$

where τ and ν are delay and Doppler variables, respectively, and $h_{\text{DD}}(\tau, \nu)$ is the DD channel response that is typically sparse [74] (a small number of reflectors with associated delays and Doppler shifts; limited number of multi-paths) and can be expressed as [74]

$$h_{\text{DD}}(\tau, \nu) = \sum_{i=1}^{N_p} h_i \bar{\delta}(\tau - \tau_i) \bar{\delta}(\nu - \nu_i), \quad (44)$$

where N_p is the number of paths, $\bar{\delta}(\cdot)$ is the Dirac delta function, and h_i , τ_i , and ν_i are the i th-path gain, delay, and Doppler shift, respectively:

$$\tau_i = \frac{l_{\tau_i}}{M \Delta f}, \quad \nu_i = \frac{k_{\nu_i}}{NT}, \quad (45)$$

for integers l_{τ_i}, k_{ν_i} (indexes of the lattice in (5)). Note that the assumptions in (45) can be further extended to involve fractional Doppler shifts, which result in additional inter-Doppler interference. The resultant performance degradation can be compensated in the equalizer, using the message-passing algorithm [74], for example. We can ignore fractional delays in a typical wideband THz system since the resolution is sufficient to approximate the path delay to the nearest point in the DD lattice [74]. The Rx signal, after discarding CP, is sampled as

$$y_{\text{OTFS}}[u] = \sum_{i=1}^{N_p} h_i e^{j2\pi \frac{k_{\nu_i}(u - l_{\tau_i})}{MN}} x_{\text{OTFS}}[[u - l_{\tau_i}]_{MN}] + n_{\text{OTFS}}[u], \quad (46)$$

$$\mathbf{y}_{\text{OTFS}} = \mathbf{H}_{\text{DD}} \mathbf{x}_{\text{OTFS}} + \mathbf{n}_{\text{OTFS}}, \quad (47)$$

where $\mathbf{y}_{\text{OTFS}} \in \mathbb{C}^{MN \times 1}$, $\mathbf{n}_{\text{OTFS}} \sim \mathcal{CN}(\mathbf{0}, \sigma_n^2 \mathbf{I}_{MN})$, and $\mathbf{H}_{\text{DD}} \in \mathbb{C}^{MN \times MN}$ is the channel matrix

$$\mathbf{H}_{\text{DD}} = \sum_{i=1}^{N_p} h_i \mathbf{\Pi}_{l_{\tau_i}} \Delta^{k_{\nu_i}}, \quad (48)$$

with $\mathbf{\Pi}_{l_{\tau_i}} \in \mathbb{R}^{MN \times MN}$ being the delay matrix, a forward cyclic shifted permutation of $\mathbf{\Pi}$ of delay l_{τ_i} ($\mathbf{\Pi}_{l_{\tau_i}=1} = \mathbf{\Pi}$ and $\mathbf{\Pi}_{l_{\tau_i}=0} = \mathbf{I}_{MN}$),

$$\mathbf{\Pi} = \begin{bmatrix} 0 & \cdots & 0 & 1 \\ 1 & \ddots & 0 & 0 \\ \vdots & \ddots & \ddots & \vdots \\ 0 & \ddots & 1 & 0 \end{bmatrix}, \quad (49)$$

and $\Delta^{k_{\nu_i}} \in \mathbb{C}^{MN \times MN}$ is the Doppler shift matrix which modulates the Tx signal with a carrier at frequency k_{ν_i} , where $\Delta = \text{diag}(\omega^0, \omega^1, \dots, \omega^{MN-1})$ and $\omega = e^{\frac{j2\pi}{MN}}$.

The Rx signal is then transformed into TF using Wigner transform, which match filters $\mathbf{y}_{\text{OTFS}}(t)$ with an Rx pulse shape, $g_{\text{rx}}(t)$, and samples it at the lattice points defined in (4). The Wigner transform is given by

$$\begin{aligned} y_{\text{TF}}[m, n] &= A_{g_{\text{rx}}, \mathbf{y}_{\text{OTFS}}}(t, f)|_{t=nT, f=m\Delta f}, \\ A_{g_{\text{rx}}, y}(t, f) &= \int g_{\text{rx}}^*(t' - t) \mathbf{y}_{\text{OTFS}}(t) e^{-j2\pi f(t'-t)} dt'. \end{aligned} \quad (50)$$

We can express (50) (similar to (41)) after building $\mathbf{Y}_{\text{OTFS}} \in \mathbb{C}^{M \times N}$ from \mathbf{y}_{OTFS} 's in (47) as

$$\mathbf{Y}_{\text{TF}} = \mathbf{F}_M \mathbf{G}_{\text{rx}} \mathbf{Y}_{\text{OTFS}}, \quad (51)$$

where $\mathbf{Y}_{\text{TF}} \in \mathbb{C}^{M \times N}$ consists of elements $y_{\text{TF}}[m, n]$. The Rx windowing operation is similar to (39). Thus, $\tilde{\mathbf{Y}}_{\text{TF}} = \text{vec}(\mathbf{\tilde{Y}}_{\text{TF}}) = \mathbf{U}_{\text{rx}} \mathbf{Y}_{\text{TF}}$ (in our case $\mathbf{U}_{\text{rx}} = \mathbf{I}_{MN}$). Then, the TF domain signal, $\tilde{\mathbf{y}}_{\text{TF}}[m, n] = y_{\text{TF}}[m, n]$, is mapped back to the DD domain using the symplectic finite Fourier transform (SFFT) as

$$y_{\text{DD}}[l, k] = \frac{1}{\sqrt{MN}} \sum_{m=0}^{M-1} \sum_{n=0}^{N-1} y_{\text{TF}}[m, n] e^{-j2\pi(\frac{nk}{N} - \frac{ml}{M})}, \quad (52)$$

$$\mathbf{Y}_{\text{DD}} = \mathbf{F}_M^H \mathbf{Y}_{\text{TF}} \mathbf{F}_N = \mathbf{F}_M^H (\mathbf{F}_M \mathbf{G}_{\text{rx}} \mathbf{Y}_{\text{OTFS}}) \mathbf{F}_N, \quad (53)$$

where $\mathbf{Y}_{\text{DD}} \in \mathbb{C}^{M \times N}$ is composed of $y_{\text{DD}}[l, k]$. We can write (53), after substituting (42) in (47), in a vectorized form

$$\begin{aligned} \mathbf{y}_{\text{DD}} &= \text{vec}(\mathbf{Y}_{\text{DD}}) = (\mathbf{F}_N \otimes \mathbf{G}_{\text{rx}}) \mathbf{y}_{\text{OTFS}} \\ &= (\mathbf{F}_N \otimes \mathbf{G}_{\text{rx}}) \mathbf{H}_{\text{DD}} (\mathbf{F}_N^H \otimes \mathbf{G}_{\text{tx}}) \mathbf{d}_{\text{DD}} + (\mathbf{F}_N \otimes \mathbf{G}_{\text{rx}}) \mathbf{n}_{\text{OTFS}} \\ &= \mathbf{H}_{\text{DD}}^{\text{eff}} \mathbf{d}_{\text{DD}} + \tilde{\mathbf{n}}_{\text{OTFS}}, \end{aligned} \quad (54)$$

where $\mathbf{H}_{\text{DD}}^{\text{eff}}$ denotes the effective channel matrix in the DD domain, and $\tilde{\mathbf{n}}_{\text{OTFS}}$ is the modified noise vector. OTFS equalization and detection can be applied directly on the vectorized form in (54), where message passing is shown to be efficient [74]. However, we only consider the linear equalizers ZF/MMSE [76] (not the low-complexity version in [76]) for a fair comparison with other candidate waveforms.

Note that M determines the delay resolution and the channel's maximum supported Doppler spread (ν_{max}) for a given

bandwidth (B); N dictates Doppler resolution and latency ($T_f = NT$). OTFS system design parameters are thus related (we only choose three from $\Delta f, T, M, N$), where $\Delta f = B/M = 1/T$ is chosen such that

$$\nu_{\text{max}} < \Delta f < 1/\tau_{\text{max}}. \quad (55)$$

Using more subcarriers (M) results in smaller SCS (Δf) for a fixed B , which in turn results in a longer slot duration (T). The OTFS design should thus observe the maximum latency constraints of novel use cases. Furthermore, the OTFS PAPR, complexity, and decoding delay are proportional to N , so lower N values are favored. However, increasing frame size (large N) results in enhanced BER performance [75] (higher diversity). Therefore, a careful trade-off between latency, PAPR, complexity, and performance is crucial with OTFS.

Table II presents maximum Doppler spread (ν_{max}) values in different bands, from below 6 GHz to THz. The noted severe changes in ν_{max} impose many challenges on both waveform design and receiver components (automatic frequency control range and synchronization). Frequency synchronization in the presence of large CFO (tens/hundreds of KHz) is challenging for CP-OFDM, even for low user mobility, where complex circuits are required at the Rx side. The resilience of OTFS to CFO and Doppler spreads reduces such complexity, which is much needed in THz communications.

L. DFT-s-OTFS

DFT-spread-OTFS [46], [47] is recently proposed for THz ISAC to improve OTFS's PAPR characteristics and enhance the robustness to Doppler effects. Although this waveform seems to be a promising candidate for many THz applications, a detailed analysis of complexity, SE, PH-E2E latency, and robustness to PHN and THz-specific impairments is still lacking. We conduct this analysis through this work to draw a fair conclusion.

The block diagram of DFT-s-OTFS is illustrated in Fig. 3(f). One DFT-s-OTFS data frame contains the same number of symbols in an OTFS frame (NM). However, for the case of one user in the uplink, only $\bar{N}M$ data symbols ($\bar{N} \leq N$) are first spread using DFT-precoding, similar to DFT-s-OFDM, followed by a DD mapping. The mapping is expressed via $\mathbf{M}_{NM, \bar{N}M}^{\text{DD}}$ of size $(NM) \times (\bar{N}M)$, which forms the data frame by concatenating the DFT-spread data into $\bar{N}M$ points and zero-padding on the remaining points $(N - \bar{N})M$ to form the DD lattice³. Then, the same operations of OTFS Tx are applied. Thus, the data matrix, \mathbf{D}_{DD} of (38), is expressed as

$$\begin{aligned} \mathbf{D}_{\text{DD}} &= \mathbf{M}_{NM, \bar{N}M}^{\text{DD}} \mathbf{F}_{\bar{N}} \bar{\mathbf{D}}_{\bar{N}M} \\ \mathbf{d}_{\text{DD}} &= \text{vec}(\mathbf{D}_{\text{DD}}) = \mathbf{M}_{NM, \bar{N}M}^{\text{DD}} (\mathbf{I}_M \otimes \mathbf{F}_{\bar{N}}) \bar{\mathbf{d}}_{\bar{N}M}. \end{aligned} \quad (56)$$

We can perform DD domain equalization for delay-Doppler domain signal estimation first, using linear equalizers (MMSE or ZF), and then perform \bar{N} -point IDFT to obtain the Tx symbols [46]. Other low-complexity solutions in [46], [47] do not guarantee a fair comparison with waveforms that use linear

³The downlink transmission is detailed in [46], alongside the uplink scenario where $\bar{K} = N/\bar{N}$ users are multiplexed along the Doppler axis.

TABLE II: Maximum Doppler spread (v_{\max}) at different terminal speeds and frequency bands

Frequency band cen. freq. f_c (Hz)	below 6 GHz		mmWave		sub-THz		THz	
	3 GHz	28 GHz	60 GHz	150 GHz	300 GHz	0.8 THz	1.2 THz	
Speed v (km/hr)								
5	14	130	278	695	1390	3706	5559	
30	83	778	1668	4170	8339	22238	33356	
120	334	3113	6671	16678	33356	88950	133426	
300	834	7783	16678	41696	83391	222376	333564	
500	1390	12972	27797	69493	138985	370627	555940	

TABLE III: Simulation parameters

Common parameters	Values
Operating frequency f_c	0.3 THz
System bandwidth B	10 GHz
Number of subcarriers M	128, 256
Number of MC/OTFS symbols N	8, 16, 32
Modulation scheme	4-QAM
Overlapping factor (PHYDYAS) O	4
DFT-s-OFDM mode	Localized
Oversampling factor L	4
Channel parameters	Values
Molecular absorption coefficient	0.0033 m^{-1}
Cluster arrival rate	0.13 nsec^{-1}
Ray arrival rate	0.37 nsec^{-1}
Cluster decay factor	3.12 nsec
Ray decay factor	0.91 nsec
Tx and Rx Antenna Elements gains	0 dB

equalizer. As illustrated in Sec. III-D, the maximum PAPR of DFT-s-OTFS is limited by \bar{N} ; an enhanced PAPR performance compared to both OTFS and CP-OFDM [46]. Moreover, due to the potential full TF channel diversity, OTFS and DFT-OTFS outperform reference MC schemes. All that emphasizes the prospects of DFT-s-OTFS in emerging V2X use cases in THz-enabled B5G/6G. However, the price to pay is in increased Rx detection and DD channel estimation complexity, as illustrated in Sec. III-C, especially in the presence of fractional Doppler [77].

IV. SIMULATION RESULTS AND DISCUSSION

This section presents the results of extensive simulations investigating relevant modulation KPIs under realistic THz conditions. The default simulation settings are listed in Table III (modifications are declared subsequently and channel parameters are taken from [52]). We list in Table V a summary of the waveform comparisons under the studied KPIs.

A. Normalized SE and PH-E2E Latency

Table IV compares the normalized SE and PH-E2E latency of the studied schemes, assuming a fixed modulation order of $\log_2(|X|)$, and a frame of MN symbols; Fig. 4 further plots the normalized SE values versus the number of subcarriers (M). Assume a target of 10 Gbps at a system bandwidth of $B = 10$ GHz, with $N_{\text{CP}} = 48$. OQAM/FBMC achieves high normalized SE for large N (asymptotic normalized SE of 1 as N goes to infinity; absence of CP) and low normalized SE for short frames (per-subcarrier pulse-shaping extends frame duration by $O - 1/2$). OTFS achieves the best normalized SE performance, outperforming both CP-OFDM and SC-FDE (mainly due to CP overhead). An additional SE loss

TABLE IV: normalized SE and PH-E2E latency of SC/MC schemes

Waveform	normalized SE	PH-E2E latency
CP-OFDM	$\frac{M}{M+N_{\text{CP}}}$	$N \times \frac{M+N_{\text{CP}}}{F_s}$
SC-FDE	$\frac{M}{M+N_{\text{CP}}}$	$N \times \frac{M+N_{\text{CP}}}{F_s}$
DFT-s-OFDM	$\frac{M}{M+N_{\text{CP}}}$	$N \times \frac{M+N_{\text{CP}}}{F_s}$
OQAM/FBMC	$\frac{N}{N+O-1/2}$	$M \times \frac{N+O-1/2}{F_s}$
OTFS	$\frac{M}{M+(N_{\text{CP}}/N)}$	$\frac{N \times M + N_{\text{CP}}}{F_s}$
DFT-s-OTFS	$\frac{MN}{MN+(N_{\text{CP}})}$	$\frac{N \times M + N_{\text{CP}}}{F_s}$

is introduced in DFT-s-OFDM where only $\bar{M} \leq M$ symbols allocated over M subcarriers (30). Moreover, using only $\bar{N}M$ data symbols ($\bar{N} \leq N$), the DFT-OTFS waveform results in a similar SE loss (56). However, such loss for DFT-s-OFDM is negligible in multi-user scenarios as vacant subcarriers can be allocated to other users, and in DFT-s-OTFS as multi-user can be multiplexed along the Doppler axis (see Fig.2). The normalized SE of CP-OFDM increases with M , where a CP-OFDM symbol transmits M QAM symbols over M subcarriers of duration $T = T_u + T_{\text{CP}}$, repeated for N symbols per frame. However, the normalized SE of CP-OFDM does not reach 1 bit/sec/Hz and is independent of N , which is an important feature for controlling the PH-E2E latency. Note that SC-FDE has the same normalized SE as CP-OFDM; we thus exclude its results (one CP for every M QAM symbols (31)).

Regarding PH-E2E latency, Fig. 5 illustrates that OTFS has lower latency than CP-OFDM, the latter which has the same latency as both SC-FDE and DFT-s-OFDM, whereas DFT-s-OTFS has the same OTFS latency. OQAM/FBMC has lower latency for smaller N and M values, but higher latency for long frame duration. The OTFS advantages, in terms of normalized SE and PH-E2E latency, are arguably due to the use of a single CP per frame of MN symbols, which can be achieved in other waveforms by considering a longer frame of the same number of MN symbols and CP length. However, it is important to emphasize that the channel is imposed, and consequently, both τ_{rms} and T_{coh} control the maximum symbol and CP duration, as shown for CP-OFDM in (29).

B. PSD and OOB

The OOB emissions and the impact of adjacent channel leakage are studied in Fig. 6 by comparing the PSD of two users utilizing various waveforms under the IEEE Tx spectral mask specifications (Sec. 13.1.3 [17]). Each user occupies a bandwidth of $B = 2.16$ GHz, with $f_c = 305.64$ GHz for the first user (ID = 25 [17]) and the second user is assigned the next channel. The results confirm that OQAM/FBMC has

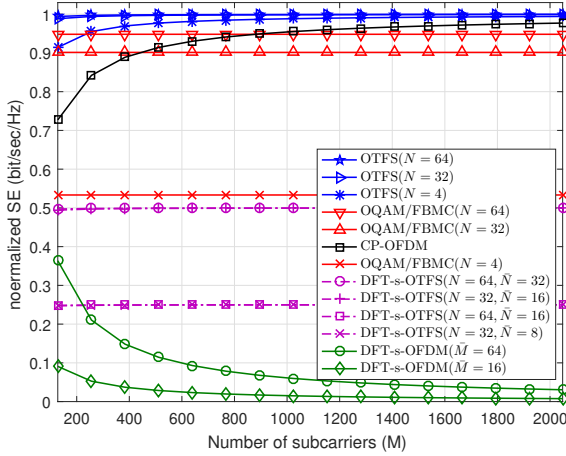


Fig. 4: Comparison of normalized SE.

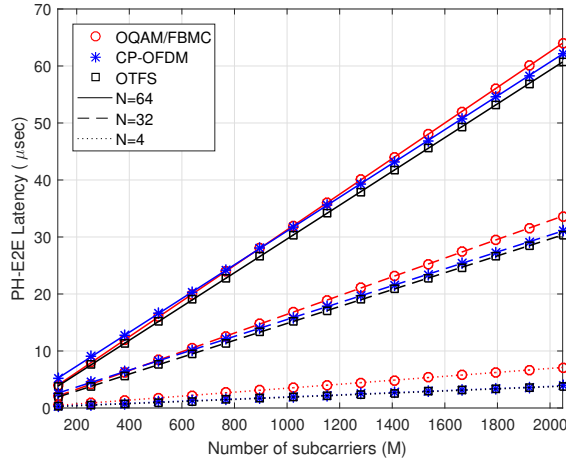


Fig. 5: Comparison of PH-E2E latency.

the best frequency localization, thanks to its pulse-shaping filter on each subcarrier; other waveforms respect the specified mask. However, it is expected that a much lower spectral emission mask will be specified for B5G/6G networks. Thus, all waveforms other than OQAM/FBMC would show a high interference level. Note that without additional pulse shaping, the OOB performances of OTFS, DFT-s-OTFS, and SC-FDE are those of CP-OFDM and DFTs-OFDM; thus excluded from Fig. 6. To ensure a fair comparison with OTFS and DFT-s-OTFS, we concatenate $N = 16$ MC/SC signals in a frame for the previous waveforms. Although DFT-s-OFDM suffers from high OOB emissions, variants such as zero-tail DFT-s-OFDM [25] could overcome this limitation. Furthermore, the performance in the presence of a pulse-shaping filter depends on parameters such as the roll-off factor, oversampling ratio, and used filter length, raised-cosine (RC) for example, (out of this work's scope). Therefore, including a guard band is crucial to achieving the required OOB and interference levels; a careful trade-off between OOB and SE needs to be maintained.

C. Complexity Analysis

The computational complexities of different waveforms (Sec. III-C) are compared in Fig. 7, for a maximum $F_s = 1$ GHz (due to hardware constraints) **but without taking into account the equalization complexity**. CP-OFDM has the same overall complexity as SC-FDE; CP-OFDM and SC-FDE enjoy lower complexities than both DFT-s-OFDM (due to additional DFT/IDFT precoding blocks in Tx/Rx) and OQAM/FBMC (due to pulse-shaping, overlapping, and OQAM processing that doubles the complexity). OQAM/FBMC is the most complex scheme compared to the previous schemes in that sense. When neglecting the equalization complexity for both OTFS and DFT-s-OTFS, Fig. 7 shows these two waveforms to be the least complex (complexity that is a function of N and \bar{N} ; not M). However, the significant part of complexity comes from the equalizer process. It is clear from the analysis in Sec. III-C that DD equalization complexity is multiple orders greater than that of other SC and MC schemes, where the state-of-the-art OTFS equalizers are much more complex than the CP-OFDM ZF/MMSE equalizers. Thus, a viable OTFS solution with low-complexity implementation and good performance, such as unitary approximate message passing (UAMP) or variational Bayes (VB) detection, is a must [63]. A low-complexity solution, compared to linear MMSE, is proposed in [47] for DFT-s-OTFS, based on the conjugate gradient method, which has an overall complexity of $\mathcal{O}(MN\log_2(MN))$; the solution still results in high complexity compared to TF MC schemes.

D. CCDF of PAPR

A comparison among the waveforms using different settings and assuming Nyquist sampling is illustrated in Fig. 8. All schemes (except OQAM/FBMC) apply rectangular pulse-shaping. SC-FDE achieves the best performance (lowest PAPR), followed by DFT-s-OFDM and DFT-s-OTFS, which outperform OTFS, CP-OFDM, and OQAM/FBMC. In particular, DFT-s-OFDM with $\bar{M} = 8$ and DFT-s-OTFS with $\bar{N} = 8$ show 3.3 dB and 3 dB PAPR gains compared to CP-OFDM at a CCDF of 10^{-3} , respectively. Furthermore, DFT-s-OFDM PAPR is dependent on M (1.8 dB increase between $\bar{M} = 8$ and $\bar{M} = 64$ at a CCDF of 10^{-3}) while DFT-s-OTFS PAPR is dependent on \bar{N} (1.2 dB increase between $\bar{N} = 4$ and $\bar{N} = 8$ at a CCDF of 10^{-3}), whereas OTFS PAPR is dependent on N (17) (2.7 dB increase between $N = 2$ and $N = 4$ at a CCDF of 10^{-3}). Note that, as expected from analysis in Sec. III-D, OTFS shows good characteristics only for small N . OQAM/FBMC is worst performing (0.9 dB worse than CP-OFDM at a CCDF of 10^{-3}) due to inherent per-subcarrier pulse-shaping. The CP-OFDM simulations are in agreement with approximation (17). However, this is not the case for OTFS as the theoretical bound in (17) is only valid for high N values [66].

The results of detailed analyses of waveform's PAPR CCDFs are illustrated in Fig. 9 for different scenarios assuming both Nyquist sampling and oversampling ($L = 4$) to provide accurate conclusions for the discrete and continuous-time signals. Figures 9a and 9b show the effect of changing N and M on PAPR, with $N = 4, M = \{32, 128, 256\}$ and $N = 32, M = \{128, 256\}$, respectively, for both $L = 1$ and

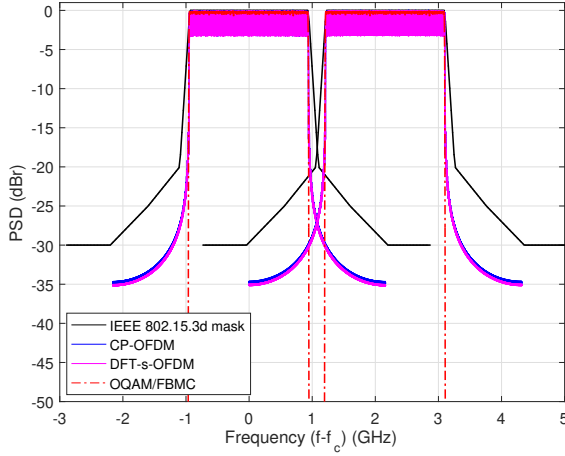


Fig. 6: Comparison of OOB emissions between two users' PSD.

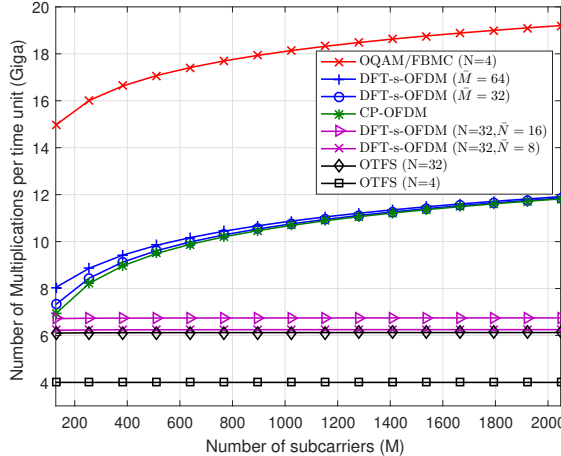


Fig. 7: Comparison of Tx/Rx computational complexity without equalization complexity.

$L = 4$; we only simulate CP-OFDM and OTFS (CP-OFDM findings also apply to OQAM/FBMC). We note that increasing either M or N increases PAPR ((16) and (17)). Nevertheless, the maximum PAPR in OTFS grows linearly with N , and the CCDF is zero for γ_{th} values greater than a threshold related to N (for example, the maximum PAPR for $N = 4$ is $10 \log(4) = 6.02$). For $L = 1$, the PAPR gap is more than 6 dB. However, this gap decreases with continuous-time signals, where the OTFS PAPR gain is no more than 1.5 dB for small N values, and is only 0.3 dB compared to CP-OFDM at a CCDF of 10^{-3} for large N values. Thus, OTFS provides significantly better PAPR than CP-OFDM only for small N values compared to M . However, OTFS still shares the high PAPR characteristics with TF MC signals. Furthermore, we demonstrate in Fig. 9b good agreement between simulated and analytical results of CP-OFDM for large N and acceptable bound of OTFS (no more than 0.5 dB difference).

The effect of pulse-shaping on PAPR performance in SC-FDE, DFT-s-OTFS, and DFT-s-OFDM is illustrated in Fig. 9c, varying the roll-off factor ($\alpha = \{0, 0.5, 1\}$) of the RC filter:

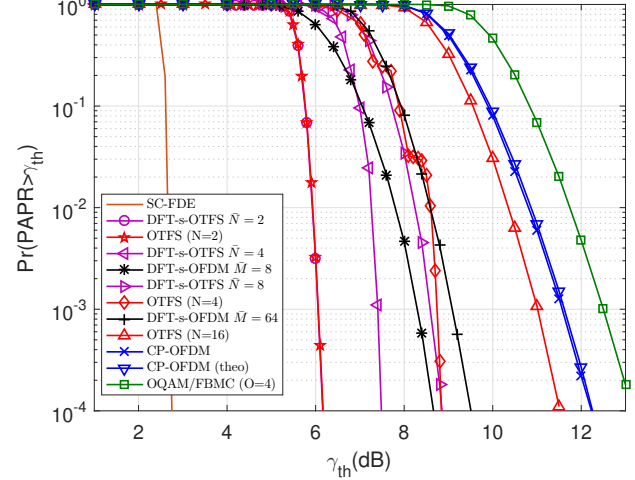


Fig. 8: Performance evaluation of PAPR CCDF among waveforms using 16-QAM, $M = 128$, $N = 16$, rectangular pulse-shaping, and Nyquist sampling.

$\frac{\cos(\pi\alpha t/T)\text{sinc}(t/T)}{(1-4\alpha^2(t/T)^2)}$ (an RC filter of 6 symbols; oversampling factor of 4; normalized to unit energy). We notice that increasing α significantly improves the PAPR performance in SC-FDE, but at the expense of excess bandwidth; DFT-s-OFDM is not as highly affected. Moreover, the PAPR variations with α are negligible for small \bar{M} values. Furthermore, DFT-s-OTFS promises low PAPR when carefully choosing \bar{N} and α .

In Fig. 9d, we show that the PAPR in DFT-s-OFDM and DFT-s-OTFS has almost the same value when the DFT precoding sizes are equal ($\bar{N} = \bar{M}$), for both Nyquist sampling ($L = 1$) and continuous-time signals ($L = 4$). Moreover, the two waveforms secure approximately 3 dB PAPR reduction compared with both OTFS and CP-OFDM.

E. Phase Noise

We first verify our assumption of Gaussian PHN for THz communications. We incorporate the PHN measurement results in [78] for a 300 GHz signal source, a PHN floor level of $K_0 = -110 \text{ dBc/Hz}$, and $K_2 = 10$ ($f_{\text{cor}} = 1 \text{ MHz}$); we set $B = 10 \text{ GHz}$, which satisfies (18). We consider Tx PHN without loss of generality. For an AWGN channel plus Tx PHN ($h[u] = 1$, for all u in (19)), the CP-OFDM results in Fig. 10a illustrate that the models in (20) and (22) are equivalent. Hence, for large bandwidths, the uncorrelated model of (22) is sufficient. The reason behind this observation is that the Wiener model PSD decreases with frequency, resulting in PHN power levels lower than the white floor noise of the Gaussian model at frequencies higher than (f_{cor}). Note that the PHN power of the Gaussian model is constant; we add a reference AWGN lower bound. PHN leads to inter-carrier interference (ICI) and adjacent channel interference, which explains the resultant degradation. The comparison assuming Gaussian PHN in Fig. 10b illustrates that DFT-s-OFDM and DFT-s-OTFS are the most robust waveforms to PHN, and decreasing \bar{M} and \bar{N} enhances the performance. Surprisingly, we demonstrate that both DFT-s-OFDM and DFT-s-OTFS

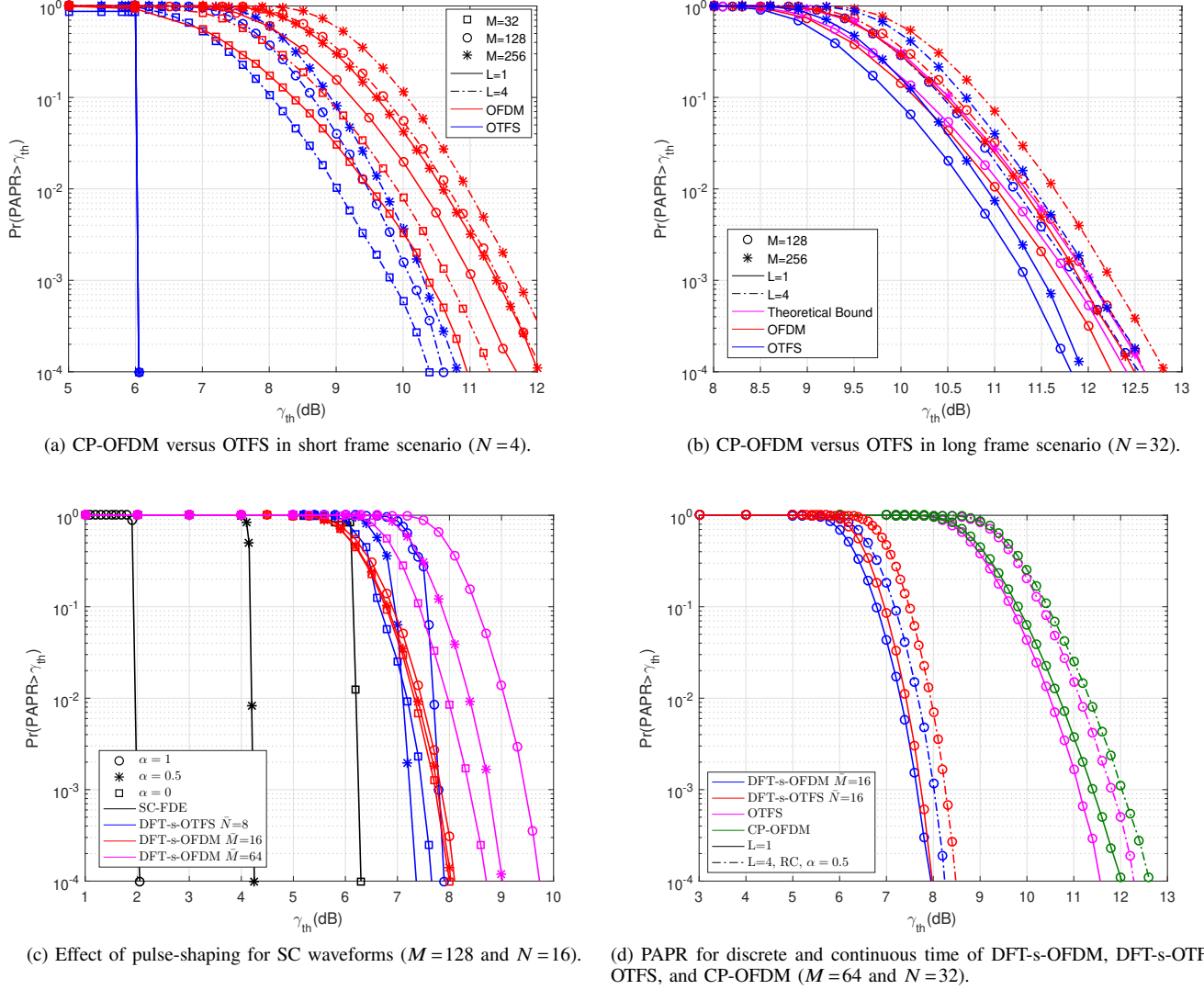


Fig. 9: PAPR CCDF comparison for different scenarios with modulation scheme 4-QAM.

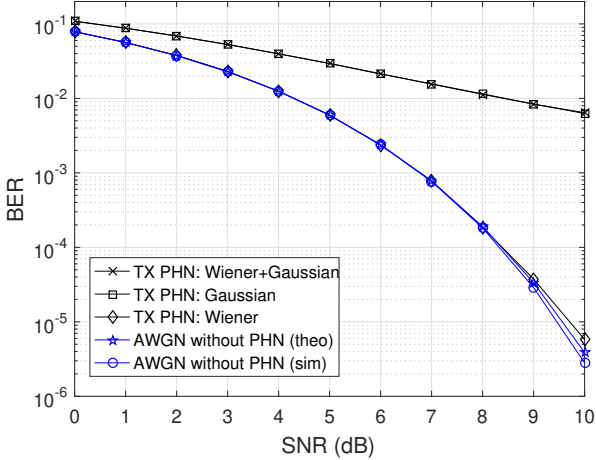
result in the same performance when the ratios M/\bar{M} and N/\bar{N} are equal. OQAM/FBMC outperforms other schemes because of its good time and frequency localization. Furthermore, CP-OFDM and OTFS are more robust than SC-FDE. SC-FDE has the worst performance. We also analyze the effect of changing the noise variance (σ_g^2) assuming THz-band Gaussian PHN and an SNR of 10 dB in Fig. 10c. We vary σ_g^2 between low (10^{-3}), medium (10^{-2}), and strong (10^{-1}) values (as indicated in Table I in [50]), retaining a system bandwidth of $B=10$ GHz; this changes the spectral density (K_0) of the white PHN floor. Increasing σ_g^2 increases the BER, where DFT-s-OFDM and DFT-s-OTFS are the best performing.

In Fig. 10d, we study the effect of changing SCS by changing $M=\{4096, 2048, 1024, 256, 64\}$ and fixing $B=10.24$ GHz. Surprisingly, the waveform BERs are retained, which is an important feature that relaxes other design parameters. For example, we can use a small M to ensure low PAPR and high PHN robustness concurrently. Such results are not observed below 6 GHz, where increasing SCS ensures high robustness

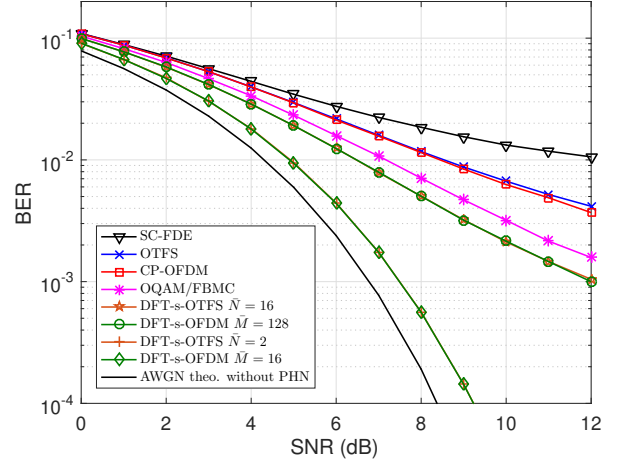
to PHN (different low-frequency models).

F. Beam Split

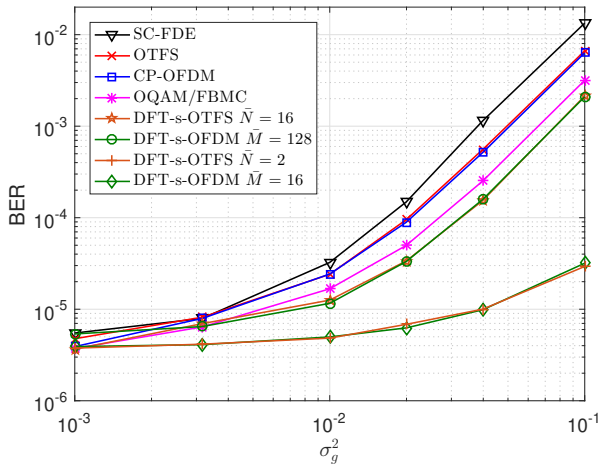
We compare all waveforms using a stochastic THz channel simulator, TeraMIMO [52], in Fig. 11, for $B=50$ GHz and $f_c=0.325$ THz. We consider an UM-MIMO system with beamforming, where both Tx and Rx have uniform linear arrays of 32 AEs; we set the communication distance to 1 m. The channel is LoS-dominant with a few multi-path components, which tends to be almost flat-fading. We first plot the BERs assuming the absence of beam split; all waveforms achieve similar performance except for OQAM/FBMC (we considered simple MMSE equalization). When adding beam split, OQAM/FBMC is shown to be less affected compared to CP-OFDM. DFT-s-OTFS, OTFS, SC-FDE, and DFT-s-OFDM (with large \bar{M}) have high robustness to THz-induced impairments, securing multiple-dB BER gains over both CP-OFDM and OQAM/FBMC.



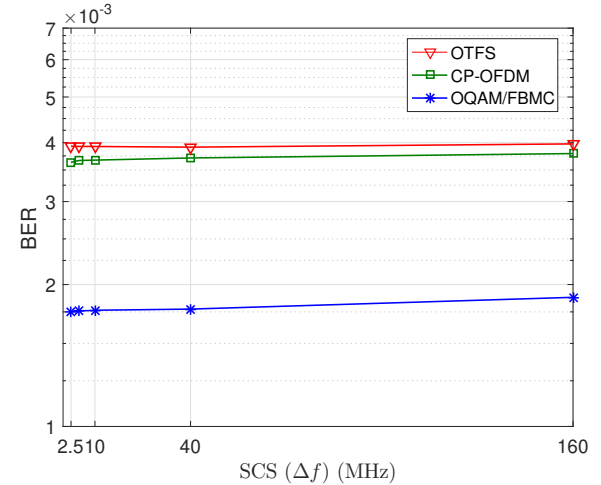
(a) CP-OFDM performance with three PHN models.



(b) Effect of Gaussian PHN model for different waveforms.



(c) Effect of changing Gaussian PHN variance at 10dB SNR.



(d) Effect of changing the SCS with Gaussian PHN.

Fig. 10: BER performance of various schemes with Tx PHN ($M=256$ and $N=32$).

G. Performance in Doubly-Selective Channels

Doppler spreads in THz channels are orders-of-magnitude larger than those in the conventional microwave and mmWave channels (Table II). In Fig. 12, we compare the BERs of the studied schemes in a doubly-selective THz channel. We consider $f_c = 0.5$ THz, $B = 0.25$ GHz, $M = 64$, $N = 16$ (for fairness between DFT-s-OTFS, OTFS and other waveforms, we concatenate N symbols per frame), and user velocity $v = \{500 \text{ km/hr}\}$. Note that the communication distance is 2 m, and cluster/rays parameters are taken from Table III (waveform parameters are derived following (55)). We consider MMSE equalization for all waveforms (other waveforms such as OQAM/FBMC show the same performance as CP-OFDM and are thus omitted). DFT-s-OTFS and OTFS more robust than CP-OFDM and other waveforms in TV-FSC, even for larger user velocity (v), showing multiple-dB BER gains. Such advantages render DFT-s-OTFS and OTFS exceptionally suitable for high-mobility, high-carrier scenarios (THz V2X scenarios, for example).

V. CONCLUSION

In this paper, a comprehensive study of SC/MC modulations for THz communications is conducted. The analysis and simulation results demonstrate that the candidate 5G waveforms (filtered-based OFDM, such as OQAM/FBMC) are not suitable for future B5G/6G networks because of the increased PAPR and complexity. Furthermore, CP-OFDM and SC-FDE share similar characteristics: good SE, moderate PH-E2E latency, high UM-MIMO compatibility, acceptable to high OOB emissions (without any additional pulse-shaping), and relatively low implementation complexity (especially with a single-tap ZF/MMSE equalizer). SC-FDE is shown to be less robust to uncorrelated Gaussian PHN, but it results in low PAPR and high robustness to THz beam split. DFT-s-OFDM is further shown to offer low PAPR and high robustness to both THz PHN and beam split. Finally, DFT-s-OTFS is illustrated to achieve high SE, low PH-E2E latency, good PAPR characteristics, and high robustness to THz impairments. However, these advantages come at the price of increased equalization

TABLE V: Performance evaluation metrics for different SC/MC waveforms

Metric \ Waveform	SC-FDE	DFT-s-OFDM	CP-OFDM	OQAM/FBMC	OTFS	DFT-s-OTFS
Spectral efficiency	medium	medium	medium	low/high	high	high
PH-E2E latency	low	medium	low/medium	high	low/medium	low/medium
UM-MIMO compatibility	high	high	high	low	high	high
PAPR	low	low/medium	high	high	medium/high	low/medium
OOB emissions	medium/high	high	high	low	high	high
Gaussian PHN robustness	low	high	low/medium	medium	low/medium	high
Beam split robustness	high	high	low	low/medium	high	high
Robustness to doubly selec. chan.	low	low	low	low	high	high
Modulator/Demodulator Complexity	medium	medium	medium	high	low/medium	low/medium
Equalization Complexity	low	low	low	medium	medium/high	high

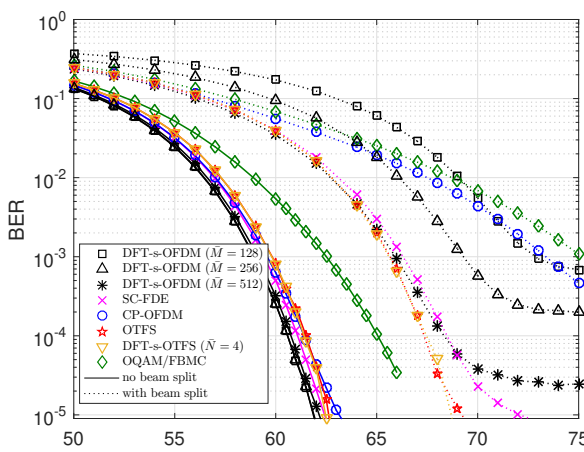
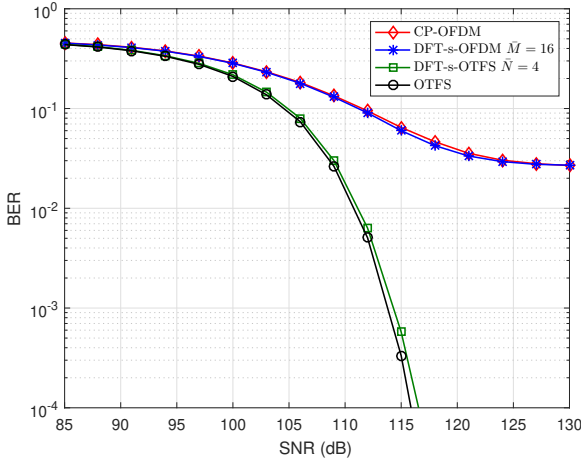
Fig. 11: BER performance of various waveforms in the presence and the absence of beam split ($M=1024$ and $N=8$).

Fig. 12: BER performance of various schemes in a THz TV-FSC.

complexity, which opens important future research directions. Furthermore, DFT-s-OTFS and OTFS outperform all other waveforms in doubly-selective channels. In a nutshell, the findings of this work recommend the use of DFT-s-OFDM and DFT-s-OTFS in B5G/6G sub-THz/THz communications; CP-OFDM can still be used in sub-THz indoor scenarios (TIV-FSC). Other relevant performance metrics can be considered in future works. For instance, researchers should study the

TABLE VI: Summary of Frequently-Used Abbreviations

Abbreviation	Definition
4G-LTE	fourth-generation long term evolution
5G-NR	fifth-generation new-radio
6G	sixth-generation
ADC	analog-to-digital converter
AE	antenna element
AFB	analysis filter bank
AoSAs	array-of-subarrays
AWGN	additive white Gaussian noise
B5G	beyond-fifth generation
BDMA	beam-division multiple-access
BER	bit error rate
CCDF	complementary cumulative distribution function
CFO	carrier-frequency offset
CP	cyclic-prefix
CPM	continuous phase modulation
CR	cognitive radio
DAC	digital-to-analog converter
DD	delay-Doppler
DFT-s-OFDM	discrete-Fourier-transform spread OFDM
DFT-s-OTFS	discrete-Fourier-transform spread OTFS
f-OFDM	filtered-OFDM
FBMC	filter-bank multi-carrier
FDE	frequency domain equalization
FDMA	frequency-division multiple-access
FFT	fast Fourier transform
FSC	frequency-selective channel
GFDM	generalized frequency-division multiplexing
ICI	inter-carrier-interference
IFFT	inverse FFT
IQI	in/quadrature-phase imbalance
ISAC	integrated sensing and communication
ISFFT	inverse SFFT
ISI	inter-symbol-interference
ITU	international telecommunications union
IRS	intelligent reflecting surface
KPI	key performance indicator
LAN	local area network
LoS	line-of-sight
MC	multi-carrier
MHz	megahertz
MMSE	minimum mean-squared error
mmWave	millimeter-wave
NLoS	non-LoS
NOMA	non-orthogonal multiple-access

waveform robustness to asynchronous access, synchronization procedures in the presence of both STO and CFO, wideband IQI, PA non-linear distortion, multi-user scheduling, and flexible resource allocation.

TABLE VII: Summary of Frequently-Used Abbreviations

Abbreviation	Definition
OFDM	orthogonal frequency-division multiplexing
OOB	out-of-band
OOK	on-off keying
OQAM	offset quadrature amplitude modulation
OTFS	orthogonal time-frequency space
PA	power amplifier
PAPR	peak-to-average power ratio
PH-E2E	physical layer end-to-end
PHN	phase noise
PS	phase-shifter
RF	radio frequency
SA	subarray
SC-FDE	single-carrier frequency-domain equalization
SCS	subcarrier spacing
SE	spectral efficiency
SFB	synthesis filter bank
SISO	single-input single-output
SS-OFDMA	spatial-spread orthogonal frequency-division multiple-access
SFFT	symplectic finite Fourier transform
STO	symbol-timing offset
Tbps	terabits-per-second
THz	terahertz
TIV	time-invariant
TV	time-variant
UFMC	universal filtered multi-carrier
UM-MIMO	ultra-massive multiple-input multiple-output
WOLA-OFDM	windowed overlap-and-add OFDM
ZF	zero-forcing

REFERENCES

[1] S. He, Y. Zhang, J. Wang, J. Zhang, J. Ren, Y. Zhang, W. Zhuang, and X. Shen, “A survey of millimeter-wave communication: Physical-layer technology specifications and enabling transmission technologies,” *Proceedings of the IEEE*, vol. 109, no. 10, pp. 1666–1705, 2021.

[2] I. F. Akyildiz, J. M. Jornet, and C. Han, “Terahertz band: Next frontier for wireless communications,” *Physical Commun.*, vol. 12, pp. 16–32, Sep. 2014.

[3] H. Elayan, O. Amin, B. Shihada, R. M. Shubair, and M.-S. Alouini, “Terahertz band: The last piece of RF spectrum puzzle for communication systems,” *IEEE Open J. of the Commun. Soc.*, vol. 1, pp. 1–32, 2019.

[4] S. Dang, O. Amin, B. Shihada, and M.-S. Alouini, “What should 6G be?” *Nature Electronics*, vol. 3, no. 1, pp. 20–29, 2020.

[5] N. Rajatheva, I. Atzeni, E. Bjornson, A. Bourdoux, S. Buzzi, J.-B. Dore, S. Erkucuk, M. Fuentes, K. Guan, Y. Hu *et al.*, “White paper on broadband connectivity in 6G,” *arXiv preprint arXiv:2004.14247*, 2020.

[6] Z. Zhang, Y. Xiao, Z. Ma, M. Xiao, Z. Ding, X. Lei, G. K. Karagiannidis, and P. Fan, “6G wireless networks: Vision, requirements, architecture, and key technologies,” *IEEE Veh. Technol. Mag.*, vol. 14, no. 3, pp. 28–41, 2019.

[7] T. S. Rappaport, Y. Xing, O. Kanhere, S. Ju, A. Madanayake, S. Mandal, A. Alkhateeb, and G. C. Trichopoulos, “Wireless communications and applications above 100 GHz: Opportunities and challenges for 6G and beyond,” *IEEE Access*, vol. 7, pp. 78 729–78 757, 2019.

[8] H. Sarieddeen, N. Saeed, T. Y. Al-Naffouri, and M.-S. Alouini, “Next generation terahertz communications: A rendezvous of sensing, imaging, and localization,” *IEEE Commun. Mag.*, vol. 58, no. 5, pp. 69–75, 2020.

[9] K. Sengupta, T. Nagatsuma, and D. M. Mittleman, “Terahertz integrated electronic and hybrid electronic-photonics systems,” *Nature Electronics*, vol. 1, no. 12, p. 622, 2018.

[10] H. Sarieddeen, M.-S. Alouini, and T. Y. Al-Naffouri, “An overview of signal processing techniques for terahertz communications,” *Proceedings of the IEEE*, vol. 109, no. 10, pp. 1628–1665, 2021.

[11] J. M. Jornet and I. F. Akyildiz, “Channel modeling and capacity analysis for electromagnetic wireless nanonetworks in the terahertz band,” *IEEE Trans. Wireless Commun.*, vol. 10, no. 10, pp. 3211–3221, 2011.

[12] G. Gougeon, Y. Corre, M. Z. Aslam, S. Bicaïs, and J.-B. Doré, “Assessment of sub-thz mesh backhaul capabilities from realistic modelling at the phy layer,” in *Proc. IEEE Euro. Conf. on Ant. and Prop. (EuCAP)*, 2020, pp. 1–5.

[13] I. F. Akyildiz, C. Han, and S. Nie, “Combating the distance problem in the millimeter wave and terahertz frequency bands,” *IEEE Commun. Mag.*, vol. 56, no. 6, pp. 102–108, 2018.

[14] A. Faisal, H. Sarieddeen, H. Dahrouj, T. Y. Al-Naffouri, and M. S. Alouini, “Ultramassive MIMO systems at terahertz bands: Prospects and challenges,” *IEEE Veh. Technol. Mag.*, vol. 15, no. 4, pp. 33–42, 2020.

[15] H. Sarieddeen, M.-S. Alouini, and T. Y. Al-Naffouri, “Terahertz-band ultra-massive spatial modulation MIMO,” *IEEE J. Sel. Areas Commun.*, vol. 37, no. 9, pp. 2040–2052, 2019.

[16] C. Han, A. O. Bicen, and I. F. Akyildiz, “Multi-ray channel modeling and wideband characterization for wireless communications in the terahertz band,” *IEEE Trans. Wireless Commun.*, vol. 14, no. 5, pp. 2402–2412, 2014.

[17] “IEEE standard for high data rate wireless multi-media networks—amendment 2: 100 Gb/s wireless switched point-to-point physical layer,” *IEEE Std. 802.15.3d-2017 (Amendment to IEEE Std. 802.15.3-2016 as amended by IEEE Std. 802.15.3e-2017)*, pp. 1–55, Oct. 2017.

[18] J. M. Jornet and I. F. Akyildiz, “Femtosecond-long pulse-based modulation for terahertz band communication in nanonetworks,” *IEEE Trans. Commun.*, vol. 62, no. 5, pp. 1742–1754, May 2014.

[19] M. S. D. Shehata, K. Wang, J. Webber, M. Fujita, T. Nagatsuma, and W. Withayachumrakul, “IEEE 802.15.3d-compliant waveforms for terahertz wireless communications,” *J. Lightw. Technol.*, 2021.

[20] J.-B. Doré, Y. Corre, S. Bicaïs, J. Palicot, E. Faussurier, D. Kténas, and F. Bader, “Above-90GHz spectrum and single-carrier waveform as enablers for efficient Tbit/s wireless communications,” in *Proc. IEEE Int. Conf. on Telecom. (ICT)*, 2018, pp. 274–278.

[21] S. Bicaïs, J.-B. Doré, G. Gougeon, and Y. Corre, “Optimized single carrier transceiver for future sub-terahertz applications,” in *Proc. IEEE Int. Conf. Acoustics, Speech, and Signal Process. (ICASSP)*, 2020, pp. 5095–5099.

[22] M. Saad, F. Bader, A. C. Al Ghouwayel, H. Hijazi, N. Bouhel, and J. Palicot, “Generalized spatial modulation for wireless terabits systems under sub-THz channel with RF impairments,” in *Proc. IEEE Int. Conf. Acoustics, Speech, and Signal Process. (ICASSP)*, 2020, pp. 5135–5139.

[23] M. Saad, J. Palicot, F. Bader, A. C. Al Ghouwayel, and H. Hijazi, “A novel index modulation dimension based on filter domain: Filter shapes index modulation,” *IEEE Trans. Commun.*, vol. 69, no. 3, pp. 1445–1461, 2020.

[24] M. Saad, N. Al Akkad, H. Hijazi, A. C. Al Ghouwayel, F. Bader, and J. Palicot, “Novel MIMO technique for wireless terabits systems in sub-THz band,” *IEEE Open J. of Vehic. Technol.*, vol. 2, pp. 125–139, 2021.

[25] A. Sahin, R. Yang, E. Bala, M. C. Beluri, and R. L. Olesen, “Flexible DFT-S-OFDM: Solutions and challenges,” *IEEE Commun. Mag.*, vol. 54, no. 11, pp. 106–112, 2016.

[26] H. Yuan, N. Yang, K. Yang, C. Han, and J. An, “Hybrid beamforming for terahertz multi-carrier systems over frequency selective fading,” *IEEE Trans. Commun.*, vol. 68, no. 10, pp. 6186–6199, 2020.

[27] C. Han, A. O. Bicen, and I. F. Akyildiz, “Multi-wideband waveform design for distance-adaptive wireless communications in the terahertz band,” *IEEE Trans. Signal Process.*, vol. 64, no. 4, pp. 910–922, Feb. 2016.

[28] Z. Hossain and J. M. Jornet, “Hierarchical bandwidth modulation for ultra-broadband terahertz communications,” in *Proc. IEEE Int. Conf. Commun. (ICC)*, 2019, pp. 1–7.

[29] H. Wang, F. Wang, H. Nguyen, S. Li, T. Huang, A. Ahmed, M. Smith, N. Mannem, and J. Lee, “Power amplifiers performance survey 2000–present,” *Georgia Tech Electronics and Micro-System Lab (GEMS), Tech. Rep.*, 2021, [Online; accessed 30-September-2021].

[30] J. Abdoli, M. Jia, and J. Ma, “Filtered OFDM: A new waveform for future wireless systems,” in *Proc. IEEE Int. Workshop on Sig. Process. Adv. in Wireless Commun. (SPAWC)*, 2015, pp. 66–70.

[31] V. Vakilian, T. Wild, F. Schaich, S. ten Brink, and J.-F. Frigon, “Universal-filtered multi-carrier technique for wireless systems beyond LTE,” in *Proc. IEEE Glob. Workshops (GC Wkshps)*, 2013, pp. 223–228.

[32] M. Bellanger, D. Le Ruyet, D. Roviras, M. Terré, J. Nossek, L. Baltar, Q. Bai, D. Waldhauser, M. Renfors, T. Ihalainen *et al.*, “FBMC physical layer: a primer,” *PHYDYAS*, vol. 25, no. 4, pp. 7–10, 2010.

[33] N. Michailow, M. Matthé, I. S. Gaspar, A. N. Caldevilla, L. L. Mendes, A. Festag, and G. Fettweis, “Generalized frequency division multiplexing for 5th generation cellular networks,” *IEEE Trans. Commun.*, vol. 62, no. 9, pp. 3045–3061, Sep. 2014.

[34] R. Zayani, Y. Medjahdi, H. Shaiek, and D. Roviras, “WOLA-OFDM: A potential candidate for asynchronous 5G,” in *Proc. IEEE Glob. Workshops (GC Wkshps)*, 2016, pp. 1–5.

[35] S. W. Tarbouche and A.-N. Assimi, "Performance of OQAM/GFDM in spatial multiplexing MIMO systems," *Int. J. of Embedded and Real-Time Commun. Syst. (IJERTCS)*, vol. 11, no. 2, pp. 39–57, 2020.

[36] A.-A. A. Boulogiorgos, E. N. Papasotiriou, and A. Alexiou, "A distance and bandwidth dependent adaptive modulation scheme for THz communications," in *Proc. IEEE Int. Workshop on Sig. Process. Adv. in Wireless Commun. (SPAWC)*, 2018, pp. 1–5.

[37] B. Zhai, A. Tang, C. Peng, and X. Wang, "SS-OFDMA: Spatial-spread orthogonal frequency division multiple access for terahertz networks," *IEEE J. Sel. Areas Commun.*, vol. 39, no. 6, pp. 1678–1692, 2021.

[38] L. You, X. Gao, G. Y. Li, X.-G. Xia, and N. Ma, "BDMA for millimeter-wave/terahertz massive MIMO transmission with per-beam synchronization," *IEEE J. Sel. Areas Commun.*, vol. 35, no. 7, pp. 1550–1563, 2017.

[39] H. Sarieddeen, A. Abdallah, M. M. Mansour, M.-S. Alouini, and T. Y. Al-Naffouri, "Terahertz-band MIMO-NOMA: Adaptive superposition coding and subspace detection," *arXiv preprint arXiv:2103.02348*, 2021.

[40] M. H. Loukil, H. Sarieddeen, M. S. Alouini, and T. Y. Al-Naffouri, "Terahertz-band MIMO systems: Adaptive transmission and blind parameter estimation," *IEEE Commun. Lett.*, vol. 25, no. 2, pp. 641–645, 2021.

[41] G. Fettweis, M. Dörpinghaus, S. Bender, L. Landau, P. Neuhaus, and M. Schlüter, "Zero crossing modulation for communication with temporally oversampled 1-bit quantization," in *53rd Asilomar Conf. on Sigs., Sys., and Computers*, 2019, pp. 207–214.

[42] R. Hadani, S. Rakib, M. Tsatsanis, A. Monk, A. J. Goldsmith, A. F. Molisch, and R. Calderbank, "Orthogonal time frequency space modulation," in *Proc. IEEE Wireless Commun. and Netw. Conf. (WCNC)*, 2017, pp. 1–6.

[43] F. Wiffen, L. Sayer, M. Z. Bocus, A. Doufexi, and A. Nix, "Comparison of OTFS and OFDM in ray launched sub-6 GHz and mmWave line-of-sight mobility channels," in *Proc. IEEE Int. Symp. Personal Indoor and Mobile Radio Commun. (PIMRC)*, 2018, pp. 73–79.

[44] G. Surabhi, M. K. Ramachandran, and A. Chockalingam, "OTFS modulation with phase noise in mmWave communications," in *Proc. IEEE Vehic. Technol. Conf. (VTC)*, 2019, pp. 1–5.

[45] Y. Wu, F. Lemic, C. Han, and Z. Chen, "A sensing integrated DFT-spread OFDM system for terahertz communications," in *Proc. IEEE Vehic. Technol. Conf. (VTC)*, 2021, pp. 1–5.

[46] Y. Wu, C. Han, and T. Yang, "DFT-spread orthogonal time frequency space modulation design for terahertz communications," in *Proc. IEEE Global Commun. Conf. (GLOBECOM)*, 2021, pp. 01–06.

[47] Y. Wu, C. Han, and Z. Chen, "DFT-spread orthogonal time frequency space system with superimposed pilots for terahertz integrated sensing and communication," *arXiv preprint arXiv:2202.10035*, 2022.

[48] Z. Sha and Z. Wang, "Channel estimation and equalization for terahertz receiver with RF impairments," *IEEE J. Sel. Areas Commun.*, vol. 39, no. 6, pp. 1621–1635, 2021.

[49] C. Lin and G. Y. Li, "Indoor terahertz communications: How many antenna arrays are needed?" *IEEE Trans. Wireless Commun.*, vol. 14, no. 6, pp. 3097–3107, 2015.

[50] S. Bicais and J.-B. Dore, "Phase noise model selection for sub-THz communications," in *Proc. IEEE Global Commun. Conf. (GLOBECOM)*, 2019, pp. 1–6.

[51] P. Neshastegaran and M. Jian, "On the effect of oscillator phase noise on the performance of OFDM systems in sub-THz band," in *Proc. Int. Conf. on Sig. Process. and Commun. Syst. (ICSPCS)*, 2020, pp. 1–6.

[52] S. Tarboush, H. Sarieddeen, H. Chen, M. H. Loukil, H. Jemaa, M. S. Alouini, and T. Y. Al-Naffouri, "TeraMIMO: A channel simulator for wideband ultra-massive MIMO terahertz communications," *IEEE Trans. Veh. Technol.*, 2021, (in press).

[53] T. Levanen, O. Tervo, K. Pajukoski, M. Renfors, and M. Valkama, "Mobile communications beyond 52.6 GHz: waveforms, numerology, and phase noise challenge," *IEEE Wireless Commun.*, vol. 28, no. 1, pp. 128–135, 2020.

[54] O. Tervo, T. Levanen, K. Pajukoski, J. Hulkko, P. Wainio, and M. Valkama, "5G new radio evolution towards sub-THz communications," in *6G SUMMIT*, 2020, pp. 1–6.

[55] T. Mao and Z. Wang, "Terahertz wireless communications with flexible index modulation aided pilot design," *IEEE J. Sel. Areas Commun.*, vol. 39, no. 6, pp. 1651–1662, 2021.

[56] S. Buzzi, C. D'Andrea, T. Foggi, A. Ugolini, and G. Colavolpe, "Single-carrier modulation versus OFDM for millimeter-wave wireless MIMO," *IEEE Trans. Commun.*, vol. 66, no. 3, pp. 1335–1348, 2017.

[57] V. Schram, Y. Wu, M. Kolleshi, and W. Gerstacker, "Comparison of transmission concepts for indoor THz communication systems," in *Proc. IEEE Int. Workshop on Mob. THz Syst. (IWMTS)*, 2020, pp. 1–5.

[58] P.-Y. Chen, C. Argyropoulos, and A. Alu, "Terahertz antenna phase shifters using integrally-gated graphene transmission-lines," *IEEE Trans. Antennas Propag.*, vol. 61, no. 4, pp. 1528–1537, 2012.

[59] M. Chafii, J. Palicot, and R. Gribonval, "Closed-form approximations of the PAPR distribution for multi-carrier modulation systems," in *Proc. Europ. Sig. Process. Conf. (EUSIPCO)*, 2014, pp. 1920–1924.

[60] Y. Xing and T. S. Rappaport, "Terahertz wireless communications: Research issues and challenges for active and passive systems in space and on the ground above 100 GHz," *arXiv preprint arXiv:2103.00604*, 2021.

[61] R. Gerzaguet, N. Bartzoudis, L. G. Baltar, V. Berg, J.-B. Doré, D. Kténas, O. Font-Bach, X. Mestre, M. Payaró, M. Färber *et al.*, "The 5G candidate waveform race: A comparison of complexity and performance," *EURASIP J. Wireless Commun. and Netw.*, vol. 2017, no. 1, pp. 1–14, 2017.

[62] A. Farhang, A. RezazadehReyhani, L. E. Doyle, and B. Farhang-Boroujeny, "Low complexity modem structure for ofdm-based orthogonal time frequency space modulation," *IEEE Wireless Commun. Lett.*, vol. 7, no. 3, pp. 344–347, 2017.

[63] Z. ZHANG, H. LIU, Q. WANG, and P. FAN, "A survey on low complexity detectors for OTFS systems," *ZTE Communications*, vol. 19, no. 4, pp. 3–15, 2022.

[64] T. Sundstrom, B. Murmann, and C. Svensson, "Power dissipation bounds for high-speed Nyquist analog-to-digital converters," *IEEE Trans. Circuits Syst. I*, vol. 56, no. 3, pp. 509–518, 2008.

[65] B. Murmann, "ADC performance survey 1997-2021," <http://web.stanford.edu/~murmann/adcsurvey.html>, [Online; accessed 30-September-2021].

[66] G. Surabhi, R. M. Augustine, and A. Chockalingam, "Peak-to-average power ratio of OTFS modulation," *IEEE Commun. Lett.*, vol. 23, no. 6, pp. 999–1002, 2019.

[67] E. Dahlman, S. Parkvall, and J. Skold, *5G NR: The next generation wireless access technology*. Academic Press, 2020, Chapter 26.

[68] M. R. Khanzadi, D. Kuylentierna, A. Panahi, T. Eriksson, and H. Zirth, "Calculation of the performance of communication systems from measured oscillator phase noise," *IEEE Trans. Circuits Syst. I*, vol. 61, no. 5, pp. 1553–1565, 2014.

[69] C.-S. Choi, "RF impairment models for 60GHz-band SYS/PHY simulation," *IEEE 802.15-06-0477-01-003c*, 2006.

[70] L. Dai, J. Tan, and H. V. Poor, "Delay-phase precoding for wideband THz massive MIMO," *arXiv preprint arXiv:2102.05211*, 2021.

[71] A. Viholainen, M. Bellanger, and M. Huchard, "Deliverable of prototype filter and structure optimization," *Criterion*, vol. 1, p. C2, 2009.

[72] A. I. Perez-Neira, M. Caus, R. Zakaria, D. Le Ruyet, E. Kofidis, M. Haardt, X. Mestre, and Y. Cheng, "MIMO signal processing in offset-QAM based filter bank multicarrier systems," *IEEE Trans. Signal Process.*, vol. 64, no. 21, pp. 5733–5762, 2016.

[73] R. Nissel, S. Schwarz, and M. Rupp, "Filter bank multicarrier modulation schemes for future mobile communications," *IEEE J. Sel. Areas Commun.*, vol. 35, no. 8, pp. 1768–1782, 2017.

[74] P. Raviteja, K. T. Phan, Y. Hong, and E. Viterbo, "Interference cancellation and iterative detection for orthogonal time frequency space modulation," *IEEE Trans. Wireless Commun.*, vol. 17, no. 10, pp. 6501–6515, 2018.

[75] G. Surabhi, R. M. Augustine, and A. Chockalingam, "On the diversity of uncoded OTFS modulation in doubly-dispersive channels," *IEEE Trans. Wireless Commun.*, vol. 18, no. 6, pp. 3049–3063, 2019.

[76] G. Surabhi and A. Chockalingam, "Low-complexity linear equalization for OTFS modulation," *IEEE Commun. Lett.*, vol. 24, no. 2, pp. 330–334, 2019.

[77] Z. Wei, W. Yuan, S. Li, J. Yuan, G. Bharatula, R. Hadani, and L. Hanzo, "Orthogonal time-frequency space modulation: A promising next-generation waveform," *IEEE Wireless Commun.*, vol. 28, no. 4, pp. 136–144, 2021.

[78] L. Yi, K. Iwamoto, T. Yamamoto, F. Ayano, A. Rolland, N. Kuse, M. Fermann, Y. Li, and T. Nagatsuma, "300-GHz-band wireless communication using a low phase noise photonic source," *Int. J. of Microwave and Wireless Tech.*, vol. 12, no. 7, pp. 551–558, 2020.